

## The Effect of Grain Size on Porewater Radiolysis

J. DeWitt<sup>1</sup>, S. McMahon<sup>2,3</sup>, and J. Parnell<sup>4</sup>

<sup>1</sup> Department of Physics, East Carolina University, Howell Science Complex, 10<sup>th</sup> Street,  
Greenville NC 27858, US

<sup>2</sup> School of Physics and Astronomy, University of Edinburgh, James Clerk Maxwell Building,  
Peter Guthrie Tait Road, Edinburgh EH9 3FD, UK

<sup>3</sup> School of Geosciences, University of Edinburgh, Grant Institute, Edinburgh EH9 3FE, UK

<sup>4</sup> School of Geosciences, University of Aberdeen, Meston Building, King's College, Aberdeen  
AB24 3UE

Corresponding authors: Joel DeWitt ([dewittjo@ecu.edu](mailto:dewittjo@ecu.edu)), Sean McMahon  
([sean.mcmahon@ed.ac.uk](mailto:sean.mcmahon@ed.ac.uk))

### Key Points:

- Porewater radiolysis in rocks and minerals yields molecular hydrogen (H<sub>2</sub>), an energy source for microbial life on Earth and perhaps Mars.
- Our Monte Carlo simulations of mineral radiation reveal how grain size controls H<sub>2</sub> yield for a give radioisotope composition and porosity.
- For some realistic scenarios, clay can produce up to an order of magnitude more H<sub>2</sub> per unit time than sand.

## Abstract

The radiolysis of porewaters by uranium, thorium, and potassium in mineral grains is a recognised source of molecular hydrogen in rock- and sediment-hosted fluids. This radiolytic hydrogen is of geomicrobiological interest as a potential energy source (electron donor) for microbial metabolism, especially in energy-limited settings such as the marine deep biosphere or the subsurface of Mars. Previous efforts to predict the production of radiolytic hydrogen from columns of rock and sediment have tended to rely upon analytic models that cannot account for the attenuation of mineral radiation by grains larger than ~30 microns. To address this, we have developed a Monte Carlo method to simulate the physics of mineral radiation and evaluate the production of H<sub>2</sub> as a function of mineral grain size and radioisotope composition. The results confirm that grain size is a major control on radiolytic H<sub>2</sub> yield. For example, using the standard geological classification of grain sizes, we find that clay can produce up to an order of magnitude more H<sub>2</sub> per unit time than sand. The magnitude of this effect is illustrated using compositional data from real geological units in order to demonstrate the dependence of radiolytic hydrogen flux on natural radionuclide concentration and bulk porosity.

## 1 Introduction

The oxidation of molecular hydrogen (hydrogenotrophy) provides energy for microbial growth in a wide variety of environments and may have sustained Earth's earliest metabolising organisms (e.g., Kral et al., 1998; Schulte et al., 2006; Sleep et al., 2011; Lane and Martin, 2012; Preiner et al., 2020). In subsurface habitats, naturally occurring H<sub>2</sub> serves as an electron donor for methanogens, acetogens, sulfate-reducers and other anaerobic microorganisms forming part of the “deep biosphere”. Analogous habitats might potentially support similar metabolisms in the deep subsurface of Mars and other planets and moons (Stevens and McKinley, 1995; Chapelle et al., 2002; Nixon et al., 2013). Although there is no direct evidence for life on these worlds as yet, methane has been detected repeatedly in the Martian atmosphere (most recently by the Curiosity rover and Mars Express Orbiter; Webster et al., 2015; Giuranna et al., 2019), and molecular hydrogen is also present in aqueous plumes venting from the subsurface ocean of Saturn's moon Enceladus (Waite et al., 2017). Hypothetically, life on these worlds might be supplied with molecular hydrogen from several natural sources also known to be active on the Earth, including organic fermentation, reactions between water and silicate minerals (known as “serpentinization”; McCollom, 1999), diffusion from crystallographic defects (Freund et al., 2002), and the reduction of water during “mechanoradical” processes driven by frictional grinding on fault planes (Hirose et al., 2011; McMahon et al., 2016). Independently of these sources, H<sub>2</sub> is produced by extremely rapid interactions between protons, electrons and radical species released from water molecules under alpha, beta and gamma irradiation issuing from radioactive elements in minerals (<sup>235</sup>U, <sup>238</sup>U, <sup>232</sup>Th, <sup>40</sup>K and their respective short-lived radiogenic daughters). Radiolysis is independent of temperature, and can generate H<sub>2</sub> from both porewater (including ice) and crystallographic water in hydrated minerals (Blair et al., 2007; Smetannikov, 2011). Water radiolysis also produces reactive oxygen species capable of oxidizing minerals to form electron acceptors such as SO<sub>4</sub><sup>2-</sup>; radiolysis can thus support microbial life at both ends of the electron transport chain (Lefticariu et al., 2010).

Several studies have attempted to model the radiolytic hydrogen ( $H_2$ ) flux from rocks and sediments beneath the seafloor and land surface under different conditions, including conditions that represent different planetary bodies. Lin et al. (2005) and Blair et al. (2007) considered crystalline continental rocks and marine shelf sediments, respectively, focusing on water-saturated pore spaces between grains, rather than fractures. Both studies used an intuitive analytical model derived from Aitken (1985) via Hofmann (1992). This model combines measured U, Th and K abundances, their activities, and reference data for the expected  $H_2$  yield from water per energy absorbed (Spinks and Woods, 1990). It accounts for the attenuation of radiation energy within the bulk medium by factoring in the radiation stopping power of water, the stopping power of the mineral grains (assumed to equal that of silica,  $SiO_2$ , which has been experimentally determined for alpha, beta and gamma radiation), and the ratio of water to mineral matter by volume (i.e., porosity). Using this model, Lin et al. showed that radiolysis is the most likely cause of high  $H_2$  concentrations measured in groundwaters of the Witwatersrand Basin in South Africa. They also modelled radiogenic  $^4He$  production and compared the predicted  $H_2:He$  ratio with the empirically measured dissolved gas concentrations in Witwatersrand groundwater; the difference showed that  $H_2$  was either produced less efficiently than the model predicted or was being consumed by a combination of abiotic reactions and hydrogenotrophic microorganisms. Onstott et al. (2006) adapted the model for Mars by substituting typical Martian values for crustal porosity and the concentration of parent nuclides. Assuming fully water-saturated basement,  $H_2$  production rates were found to be comparable to crystalline basement on Earth because of the higher porosity of Mars' crust, despite the lower concentrations of uranium and thorium. Updated (higher) radionuclide concentrations were used by Tarnas et al. (2018, 2021) to estimate an even greater rate of radiolytic  $H_2$  production on Mars, using the same model. Bouquet et al. (2017) applied a similar model to Jupiter's moon, Europa. Dzaugis et al. (2016) introduced a model of radiolytic  $H_2$  production from water hosted within planar fractures in radioactive rock, rather than intergranular pore spaces, and applied it to subseafloor basaltic basement. Dzaugis et al. (2018) showed that this fracture-based model yields radiolytic  $H_2$  production rates for Martian basaltic crust broadly comparable to those predicted for fine-grained Martian sediments by the model of Blair et al. (2017). One implication of these studies, in agreement with other considerations, is that the best place to seek extant life on Mars today is probably the subsurface (e.g., Tarnas et al., 2021).

Hitherto, studies of porewater radiolysis have not properly accounted for the attenuation of each radiogenic particle or ray within its mineral grain (clast or crystal) of origin. This attenuation can be safely ignored when the grain diameter is much smaller than the stopping distance of the relevant particle in the mineral medium, as for example in clay. However, alpha particles in the kinetic energy range characteristic of mineral radiation ( $\sim 5.6$  MeV on average) typically have stopping distances in  $SiO_2$  (and similar materials) of  $\sim 23$   $\mu m$  (National Institute of Standards and Technology, 2021a). Consequently, if such an alpha particle is produced near the edge of a grain of diameter  $\gtrsim 20$   $\mu m$  (i.e., coarser than a medium silt) and travels towards the interior of the grain, it will not have enough kinetic energy to escape from the other side, resulting in a null contribution to the radiolysis of the surrounding porewater. Similar considerations apply to beta particles—although their stopping distances are substantially larger—given a characteristic mean kinetic energy of  $\sim 0.33$  MeV, equating to a stopping distance of  $\sim 452$   $\mu m$  in  $SiO_2$  (National Institute of Standards and Technology, 2021b). Furthermore, the radiolysis contribution due to gamma (photon) radiation requires special treatment given their chargeless, massless character. Here, we quantitatively account for the variability of grain size in

order to expand the range of environments in which radiolytic  $\text{H}_2$  production and its potential contribution to microbial productivity can be estimated. The method detailed in this paper is generalizable to the extent that it can be adapted for a variety of geological contexts and sediment or rock types with any level of radioactivity, whose constituent grains can be of arbitrary size and shape. In this particular study, we seek to model radiolytic  $\text{H}_2$  production from porous rocks and sediments with grain sizes  $\geq 20 \mu\text{m}$  for the first time (to our knowledge). One motivation for doing so is the fact that high concentrations of radioactive minerals on Earth commonly occur in relatively coarse sedimentary rocks, e.g., sandstone-type uranium deposits. In addition, relatively coarse granular materials can accommodate more microorganisms, which may tend to be excluded by the restrictive pore throat sizes of finer-grained materials, even at the same porosity (e.g., Krumholz et al., 1997).

## 2 Materials and Methods

We have written a Fortran program that numerically simulates the physics of natural radioactive decay within a matrix of water and mineral grains, which for simplicity are assumed to be spherical and composed of pure  $\text{SiO}_2$ . (The algorithmic foundation of this program is given in [Supplementary Information S1](#).) The modeling of spherical grains allows one to leverage the rotational symmetry of the system, which has the effect of easing the conceptual and computational aspects of the Monte Carlo (MC) method. The primary goal of our simulations is to score the total amount of kinetic energy transferred to the surrounding water layer due to the decay of radioactive isotopes within  $\text{SiO}_2$  grains. [Figure 1](#) shows the geometry of a spherical  $\text{SiO}_2$  grain and a composite of sample thorium decay events occurring within it.

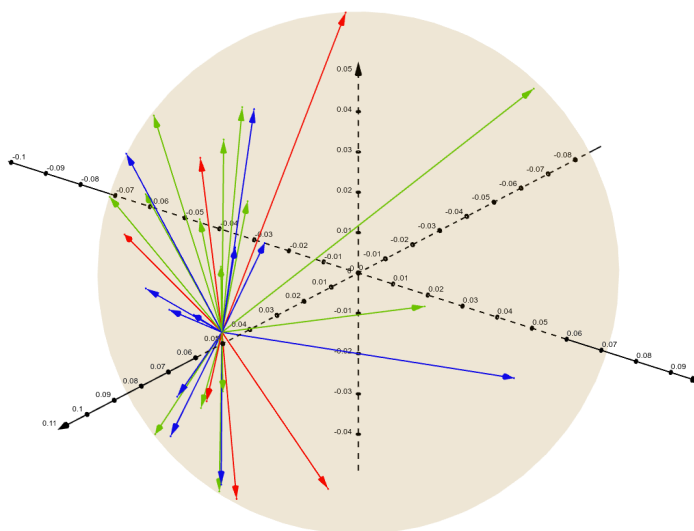


**Figure 1.** A randomly selected  $\text{SiO}_2$  grain of radius 0.059 cm (590  $\mu\text{m}$ ) showing a sample thorium decay against  $x$ ,  $y$  and  $z$  co-ordinate axes (black arrows with gradations). Alpha, beta,

and gamma decay events register as red, green, and blue, respectively. These depth vectors locate exit points that correspond to solutions of the sphere  $r^2 = x^2 + y^2 + z^2$ .

The program leverages the MC method and the physics of radioactive decay to drive a given simulation towards a well-averaged endpoint. The steps the simulation uses are as follows:

1. Choose a random SiO<sub>2</sub> grain whose radius is within the desired interval of clay, silt, or sand (Wentworth, 1922), or a logarithmic distribution of all three;
2. Choose a random K, Th, or U constituent (weighted by the proportion of that element in the composition; see “Activity of Bulk Rock or Sediment” below);
3. Choose a random point  $(x, y, z)$  within the grain at which the decay of the constituent plus its daughters will proceed;
4. Examine the entire decay chain in order, choosing random exit vectors, and applying the appropriate physics of alpha, beta, and gamma propagation in SiO<sub>2</sub>;
5. Repeat Steps 1 – 4 many times (typically 10<sup>5</sup> trials) in order to ensure the simulation converges while keeping a running total of the amount of kinetic energy (in MeV) deposited in the surrounding water layer;
6. Output radiolytic H<sub>2</sub> production from the volume of rock or sediment;
7. Using Step 6 as a baseline, scale H<sub>2</sub> production by volume-corrected porosity (see “Porosity” below). Athy’s law can be used to scale radiolytic H<sub>2</sub> production in the case where porosity can be estimated for a column of rock or sediment as a function of depth.

The “length” of the simulation is controlled by the number of K, Th, and U decays + daughters that are tracked (read: trials), with the understanding that a large number of trials will enable the simulation to converge in a manner dictated by the physics of radioactive decay. For the purposes of this study, our simulations output 1) H<sub>2</sub> production in units of moles per [Earth] year-cm<sup>3</sup> as a function of sediment depth in meters, or 2) H<sub>2</sub> production as a function of grain size (logarithmically distributed) in cm.

## 2.1 Radioactive decay

This section describes how the components of natural radioactivity interact with the medium through which they are propagating. This is also referred to as *stopping power* or *linear energy transfer* (LET). Our simulations treat alpha, beta, and gamma decay piecewise, wherein each decay daughter in a given chain is assigned a random exit vector. The entire decay chains for  $^{238}\text{U}$ ,  $^{235}\text{U}$ ,  $^{232}\text{Th}$ , and  $^{40}\text{K}$  were hard-coded into the program using data from the Interactive Chart of Nuclides provided by Brookhaven National Laboratory (2021). (The *average* energies required for each transition within a given decay chain were implemented rather than the “endpoint” or maximum energies, as previous studies have done.) These vectors are then used to propagate each decay product through a geometrically-computed depth of  $\text{SiO}_2$  material before depositing the remainder of its kinetic energy in the surrounding water layer. This strategy is advantageous since it avoids the assumption of alpha, beta, and gamma dominance through the use of lump energy sums (Blair et al., 2007).

### 2.1.1 Alpha particles

The interaction of a heavy charged projectile with the electrons in a stopping medium (absorber) is described by the Bethe-Bloch formula (Bethe, 1930). The amount of kinetic energy  $dE$  imparted to the target medium per unit path length  $dx$  is given as

$$-\left\langle \frac{dE}{dx} \right\rangle = \underbrace{\left( \frac{e^2}{4\pi\epsilon_0} \right)^2}_{\text{Coulomb}} \underbrace{\frac{4\pi Z^2}{m_e c^2 \beta^2}}_{\text{projectile}} \underbrace{\frac{\rho Z N_A}{A}}_{\text{target}} \left[ \ln \left( \frac{2m_e c^2 \beta^2}{I(1 - \beta^2)} \right) - \beta^2 - \frac{\delta}{2} \right] \quad (1)$$

where  $e^2/4\pi\epsilon_0$  is the coupling strength of electromagnetism,  $Z$  is the atomic number of the charged particle or ion projectile,  $m_e c^2$  is the rest mass-energy of the electron,  $\rho Z N_A / A$  is the electron density of the absorber with effective atomic number  $Z$  and effective atomic mass  $A$  (when referring to compounds and mixtures), and  $I$  is the mean ionization potential of the target medium. The dimensionless number  $\beta \equiv v/c = \sqrt{1 - [m_e c^2 / (E + m_e c^2)]^2}$  from special relativity. The last term in the square brackets  $\delta/2$  is the *density effect correction* that accounts for the phenomenon that, in a dense medium, the field which perturbs electrons far from the projectile track is modified by the dielectric polarization of the atoms between the distant electrons and the projectile (Fermi, 1940). The quantity  $dE/dx$  in [Equation 1](#) is sometimes preceded by a negative sign to indicate that kinetic energy is transferred to the stopping medium.

Alpha particles (helium nuclei,  $Z = 2$ ) that are emitted during the course of natural radioactive decay possess an average kinetic energy that is relatively low, or  $\sim 5.6$  MeV. This low kinetic energy necessitates a correction to the stopping power due to the phenomenon of *electron capture*, which accounts for the fact that the bare nuclear charge of the projectile is reduced and can thus be replaced by an effective projectile charge (Weaver and Westphal, 2002). Once corrected, [Equation 1](#) is used to numerically propagate alpha particles through a known amount of  $\text{SiO}_2$  with characteristics  $\rho Z N_A / A$  and  $I$ .

A charged particle or ion projectile with atomic number  $Z$  of rest mass significantly larger than that of the electron (charge  $e$ ) is considered a “heavy” charged particle. This would include mesons, protons, alpha particles, and higher  $Z$  nuclei. Electrons and positrons are considered “light” charged particles; the physics of electron propagation through matter is discussed in the next section.

### 2.1.2 Beta particles

While the Bethe-Bloch formula can be used in principle to calculate the stopping power of any charged particle passing through matter, it must be modified in the case of beta particles (electrons). There are several reasons for this:

- one must always consider special relativity when handling electron-electron interactions;
- an electron that acts as a projectile can lose nearly all of its kinetic energy in a single interaction with a target electron;
- quantum mechanics states that we will not be able to distinguish between the projectile and the target electrons after the *collision* (they are identical particles);
- for a high energy electron that traverses a high  $\bar{Z}$  stopping medium, radiative processes such as *bremstrahlung* (from the German: “breaking radiation”) will be significant.

The total stopping power of an electron as a function of kinetic energy in a specified target material is the sum of the collision plus bremsstrahlung contributions (Bethe and Heitler, 1934):

$$\left\langle \frac{dE}{dx} \right\rangle = \left\langle \frac{dE}{dx} \right\rangle_c + \left\langle \frac{dE}{dx} \right\rangle_b, \quad (2)$$

where  $\langle dE/dx \rangle_c$  is the stopping power due to electron collisions,

$$\begin{aligned} -\left\langle \frac{dE}{dx} \right\rangle_c &= \overbrace{\left( \frac{e^2}{4\pi\epsilon_0} \right)^2}^{\text{Coulomb}} \overbrace{\frac{2\pi}{m_e c^2 \beta^2}}^{\text{projectile}} \overbrace{\frac{\rho Z N_A}{A}}^{\text{target}} \\ &\times \left[ \ln \left( \frac{E(E + m_e c^2)^2 \beta^2}{2I^2 m_e c^2} \right) - \beta^2 + 1 - \left( 2\sqrt{1 - \beta^2} + \beta^2 - 1 \right) \ln 2 + \frac{1}{8} \left( 1 - \sqrt{1 - \beta^2} \right)^2 \right] \end{aligned}$$

(3)

and  $\langle dE/dx \rangle_b$  is the stopping power due to electron bremsstrahlung,

$$\underbrace{-\left\langle \frac{dE}{dx} \right\rangle_b}_{\text{bremsstrahlung}} = \underbrace{\left( \frac{e^2}{4\pi\epsilon_0} \right)^2}_{\text{Coulomb}} \underbrace{\frac{\alpha(E + m_e c^2)}{(m_e c^2)^2}}_{\text{projectile}} \underbrace{\frac{\rho \bar{Z}^2 N_A}{A}}_{\text{target}} \left[ 4 \ln \left( \frac{2(E + m_e c^2)}{m_e c^2} \right) - \frac{4}{3} \right] \quad (4)$$

228

229 where  $\alpha$  is the fine-structure constant. Equations 2-4 are used to numerically propagate beta  
 230 particles through a known amount of SiO<sub>2</sub> with characteristics similar to those described by  
 231 [Equation 1](#).

232 The simulation of radioactive decay in a mineral medium requires that Equations 1-4 be  
 233 applied to the propagation of alpha and beta particles inside spherical SiO<sub>2</sub> grains. As a means of  
 234 developing and validating our numerical method, it would be well if the algorithm given in  
 235 [Supplementary Information S1](#) were checked against a pure geometric argument. To this end, we  
 236 have found analytically that if particles with stopping distance  $s$  are emitted at random vectors  
 237 from points inside a spherical grain of diameter  $\Theta$ , the proportion (or percent fraction) of these  
 238 particles that escape from the grain rather than terminating (or stopping) within it is given by

239

$$E_g(\Theta) = \frac{3s}{2\Theta} - \frac{s^3}{2\Theta^3}. \quad (5)$$

240

241 [Equation 5](#) is derived in [Supplementary Information S2](#). [Figure 2](#) shows a graphical  
 242 comparison of these two methods in the case of alpha particles, along with an extension to beta  
 243 particles using the same algorithm given in [Supplementary Information S1](#).



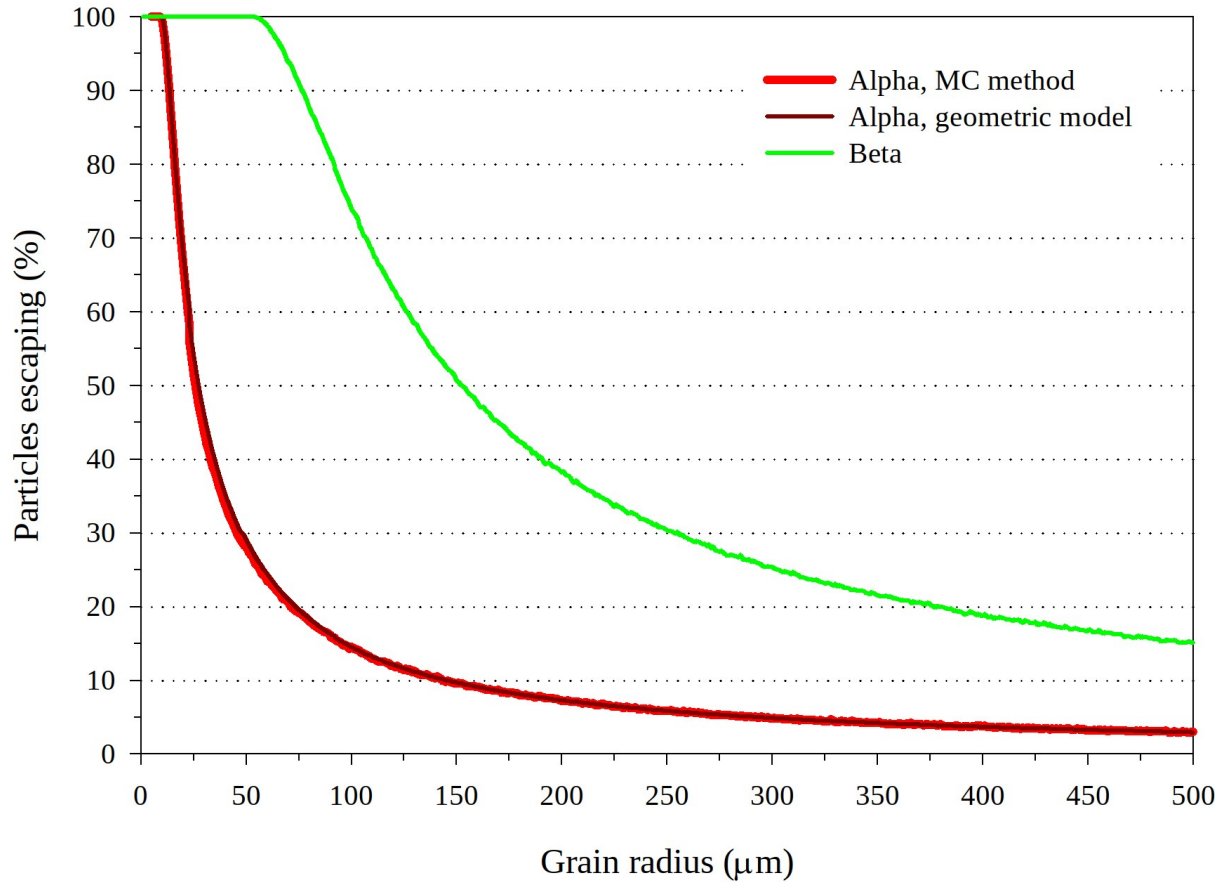


**Figure 2.** Escape efficiency of alpha particles with stopping distance  $s = 19.6 \mu\text{m}$  as a function of spherical grain radius, where the methods of Monte Carlo simulation and geometric analysis are compared. The escape efficiency of beta particles is also shown using the same algorithm.

The comparison shown in [Figure 2](#) corresponds to an alpha particle test case with stopping distance  $s = 19.6 \mu\text{m}$  (kinetic energy: 4.93 MeV). These curves disagree on average by 0.2% over 100,000 trials per micron radius. The good agreement between the core algorithm of the simulation and our geometric analysis partially validates our MC approach in this study.

### 2.1.3 Gamma Rays

Unlike energetic charged particles which have a finite range when traversing matter, gamma rays (photons) of a given energy do not possess such a discrete range, but rather are absorbed exponentially as a function of distance in the absorbing medium. This phenomenon is referred to as *attenuation*. (Alpha and beta particles, strictly speaking, do not attenuate; we use this term contextually to service the reader.) For a beam of  $n_0$  monoenergetic photons, the rate of absorption of the photons as a function of depth in the absorber is

$$-\frac{dn}{dx} = N\sigma n_0, \quad (6)$$

where  $\sigma$  is the absorption cross section of each atomic scattering center (or absorbing molecule), and  $N$  is the volume density of atomic scattering centers. (The negative sign above represents absorption.) We define  $\mu \equiv N\sigma$ , where  $\mu$  is referred to as the *linear attenuation coefficient*. We can then integrate [Equation 6](#) with respect to distance  $x$  to obtain

$$n(x) = n_0 e^{-\mu x}. \quad (7)$$

Similarly, if we consider depth  $x$  in terms of not distance, but of areal density (in g/cm<sup>2</sup>), we can define the *mass attenuation coefficient* such that

$$\mu_m \equiv \frac{\mu}{\rho} = \frac{N\sigma}{\rho} = \frac{N_A \sigma}{\bar{A}}, \quad (8)$$

where  $\rho$  is the mass density (in g/cm<sup>3</sup>),  $\bar{A}$  is the atomic molar mass (in g/mol) of the absorbing medium, and  $N_A$  is Avogadro's number (in molecules/mol), respectively. [Equation 7](#) now becomes

$$n(x) = n_0 e^{-\mu_m x}, \quad (9)$$

where the values of  $\mu_m$  are tabulated.

Using [Equation 9](#), a characteristic *attenuation* (or *absorption*) *length* can be formulated as an analog to the stopping distance of alpha and beta particles; for a single photon, this is taken as the distance  $x$  into a material when the probability of absorption has dropped to  $n/n_0 = 1/e$ , or ~37%. Explicitly, this gives a propagation distance that is equal to the inverse of the mass attenuation coefficient, or  $1/\mu_m$ . A typical attenuation length in this study is on the order of centimeters.

There are a number of different mechanisms by which photons can interact with matter. However, only three of these mechanisms—the photoelectric effect, Compton scattering, and electron/positron pair production—dominate, while the remainder usually make only a negligible contribution. The total absorption cross section  $\sigma$  in [Equation 8](#) is the sum of the cross sections for each type of photon interaction:

$$\sigma = \sigma_{PE} + \sigma_C + \sigma_{PP}, \quad (10)$$

where  $\sigma_{\text{PE}}$  is the cross section for photoelectric interactions,  $\sigma_{\text{C}}$  is the cross section for Compton interactions, and  $\sigma_{\text{PP}}$  is the cross section for pair production. (A cross section in nuclear physics can informally be read as an energy-dependent probability for interaction.) Since  $\mu \propto \sigma$  from [Equation 8](#), there is a corresponding mass attenuation coefficient for each cross section.

### 2.1.3.1 Photoelectric Effect

Free electrons cannot fully absorb photons without violating conservation of energy and conservation of momentum, and for that reason, free electrons are not subject to the photoelectric effect. Indeed, the photoelectric effect should be thought of as interaction between an incident photon and an entire atom, not just one of its electrons (Einstein, 1905).

Photoelectric interactions are more likely to eject electrons from the more tightly bound inner electron shells of the atom than the less tightly bound outer shells, since interactions involving inner shell electrons occur closer to the center of the atom where it is easier to transfer an incident photon's linear momentum to the atom. This is because nearly all the mass of the atom is concentrated in its nucleus.

The cross section for the photoelectric effect is:

$$\sigma_{\text{PE}} = 4\sqrt{2}\alpha^4 \bar{Z}^5 \frac{8\pi r_e^2}{3} \left( \frac{m_e c^2}{E_\gamma} \right)^{7/2}, \quad (11)$$

where  $\alpha$  is the fine-structure constant,  $\bar{Z}$  is the atomic number of the absorbing medium,  $r_e$  is the classical electron radius, the quantity  $m_e c^2$  is the rest mass-energy of the electron, and finally  $E_\gamma$  is the kinetic energy of the incident photon. [Equation 11](#) should be applied if the energy of the incident photon is between 0.1 and 0.35 MeV, or where the photon energy is above the K-absorption edge.

### 2.1.3.2 Compton Scattering

The interaction of photons with “nearly” free electrons is described by a number of mechanisms:

- Photon interactions with “truly” free electrons is referred to as *Thomson scattering*;
- Coherent (or elastic) photon interactions with “nearly” free electrons is referred to as *Rayleigh scattering*;
- Incoherent (or inelastic) photon interactions with “nearly” free electrons is referred to as *Compton scattering*.

Conservation of energy for the Compton scattering interaction gives

$$E_{\gamma} + m_e c^2 = E'_{\gamma} + \frac{m_e c^2}{\sqrt{1 - \beta^2}}, \quad (12)$$

where  $\beta \equiv v/c = \sqrt{1 - [m_e c^2 / (E_{\gamma} - E'_{\gamma} + m_e c^2)]^2}$  from special relativity, with  $E_{\gamma}$  and  $E'_{\gamma}$  the kinetic energies of the incident and scattered photon, respectively. After obtaining the differential cross section for Compton scattering—which is specified by the Klein-Nishina formula (Klein and Nishina, 1929)—it can be shown that integration over all angles gives the cross section for the Compton interaction:

$$\sigma_C = \frac{\pi r_e^2}{\bar{E}} \left[ \left( 1 - \frac{2(\bar{E} + 1)}{\bar{E}^2} \right) \ln(2\bar{E} + 1) + \frac{1}{2} + \frac{4}{\bar{E}} - \frac{1}{2(2\bar{E} + 1)^2} \right], \quad (13)$$

where  $\bar{E}$  effectively compares the incident photon energy to the rest mass-energy of the electron, or  $E_{\gamma}/m_e c^2$ .

### 2.1.3.3 Pair Production

Pair production is essentially the reverse process of bremsstrahlung. When in close proximity to a heavy nucleus, a photon can be converted into an electron/positron pair. Conservation of energy for this process dictates

$$E_{\gamma} = T_e + m_e c^2 + T_p + m_e c^2, \quad (14)$$

where  $T_e$  and  $T_p$  are the kinetic energy of the electron and positron, respectively. Because the rest mass of the electron and the positron must come from the energy of the photon, there is a threshold energy of  $2m_e c^2 = 1.022$  MeV below which this process cannot occur.

The cross section for pair production originates from quantum electrodynamics, and is given by (Gould and Schröder, 1967):

$$\sigma_{PP} = \frac{\pi r_e^2}{2} (1 - \beta^2) \left[ (3 - \beta^4) \ln \left( \frac{1 + \beta}{1 - \beta} \right) - 2\beta(2 - \beta^2) \right], \quad (15)$$

where  $\beta \equiv v/c = \sqrt{1 - [m_e c^2 / (E + m_e c^2)]^2}$  from special relativity. In this case  $E$  is actually the relativistic kinetic energy of the electron/positron in the center-of-mass frame of reference. This cross section is applied for the transitions  $^{40}\text{K} \rightarrow ^{40}\text{Ar}$  in  $^{40}\text{K}$  (1.461 MeV),  $^{208}\text{Tl} \rightarrow ^{208}\text{Pb}$  in  $^{232}\text{Th}$  (3.376 MeV), and  $^{214}\text{Bi} \rightarrow ^{214}\text{Po}$  in  $^{238}\text{U}$  (1.476 MeV).

## 2.2 Activity of Bulk Rock or Sediment

The activity per unit volume  $A_{\text{vol}}$  of bulk rock/sediment in units of Bq/cm<sup>3</sup> is given by

$$A_{\text{vol}}(\rho, N_{\text{ppm}}) = \frac{\rho N_{\text{A}}}{M} \frac{N_{\text{ppm}}}{10^6} \frac{\ln(2)}{t_{1/2}}, \quad (16)$$

where  $\rho$  is the mass density of the rock/sediment constituents in g/cm<sup>3</sup>,  $N_{\text{A}}$  is the Avogadro constant,  $M$  is the molar mass of the radioisotope,  $N_{\text{ppm}}$  is the concentration of the radioisotope in parts per million (ppm), and  $t_{1/2}$  is the half-life of the radioisotope in seconds. Equation 16 is used to convert the concentration of a given radioisotope component (uranium, thorium, or potassium) to the volume-normalized activity in bulk sediment/rock. For example, sediment of mass density 2.6 g/cm<sup>3</sup> that contains radioisotope concentrations of uranium (7.4 ppm), thorium (2.8 ppm), and potassium (1.3%) results in  $A_{\text{vol}}$  values of 0.24, 0.030, and 1.1 Bq/cm<sup>3</sup>, respectively, using Equation 16 and the data given in Table 1. Recognizing also that <sup>235</sup>U contributes to the overall activity (0.011 Bq/cm<sup>3</sup>), the total activity per unit volume of the sediment is simply the sum of the individual activities, or ~1.4 Bq/cm<sup>3</sup>.

**Table 1.** A summary of radioisotopes relevant to natural radioactive decay in minerals.

| Radioactive Isotope   | Molar Mass, $M$ (g/mol) | Half-life, $t_{1/2}$ (s) |
|---|-------------------------|--------------------------|
| <sup>238</sup> U (99.274%)                                      | 238.0508                | 1.4090E17                |
| <sup>235</sup> U (0.720%)                                       | 235.0439                | 2.2195E16                |
| <sup>232</sup> Th   | 232.0381                | 4.4308E17                |
| <sup>40</sup> K (0.0117% of <sup>40</sup> K in <sup>39</sup> K) | 39.0983                 | 3.9452E16                |

From an MC perspective, it is helpful to convert the  $A_{\text{vol}}$  values above to algorithm-friendly percent fractions of roughly 18%, 1%, 2%, and 79% for <sup>238</sup>U, <sup>235</sup>U, <sup>232</sup>Th, and <sup>40</sup>K, respectively. Through this example we can see that a random number generator will select potassium predominantly over the course of a given simulation.

## 2.3 Porosity

A porosity correction is needed to account for the fact that only the kinetic energy deposited in the intergranular water (rather than other grains) will contribute to H<sub>2</sub> production. The porosity of a compressible rock or sediment column decreases with increasing depth as the grains are compacted together. The simulations presented in this paper assume that all the porosity is occupied by water; we use Athy's law to quantify porosity  $\phi$  as a function of sediment (or rock) depth  $z$  (Fowler and Yang, 1998):

$$\phi(z) = \phi_0 e^{-kz}, \quad (17)$$

384

385 where  $\phi_0$  is the porosity near the surface and  $k$  is the compaction coefficient and has units of  $\text{m}^{-1}$ .  
 386 In sandstones on Earth,  $k$  takes an average value close to  $5.3\text{E-}4 \text{ m}^{-1}$  (McMahon and Parnell,  
 387 2014); for geological features on Mars, this study uses a slightly lower compaction coefficient of  
 388  $3.5\text{E-}4 \text{ m}^{-1}$  (Clifford et al., 2010). Equation 17 represents a steady-state leading-order solution to  
 389 equilibrium compaction.

390 A volume correction factor is required to properly scale  $\text{H}_2$  production as a function of  
 391 depth. This factor,  $1 - \phi_0$ , accounts for the fact that in a given volume of rock/sediment, a large  
 392 porosity will translate to a smaller proportion being occupied by radioactive mineral grains rather  
 393 than water. The kinetic energy yield from a given volume of wet rock/sediment is equal to the  
 394 energy yield of each grain (supplied by the simulation) multiplied by the total number of grains  
 395 contained in the volume. This total grain number is equal to the volume of the rock/sediment  
 396 multiplied by a factor of  $1 - \phi_0$ , normalized by the volume of each grain (Blair et al., 2007).  
 397 Given this, it is necessary to replace  $\phi_0$  in Equation 17 with  $\phi_0(1 - \phi_0)$  to give an effective  
 398 porosity as a function of rock/sediment depth.

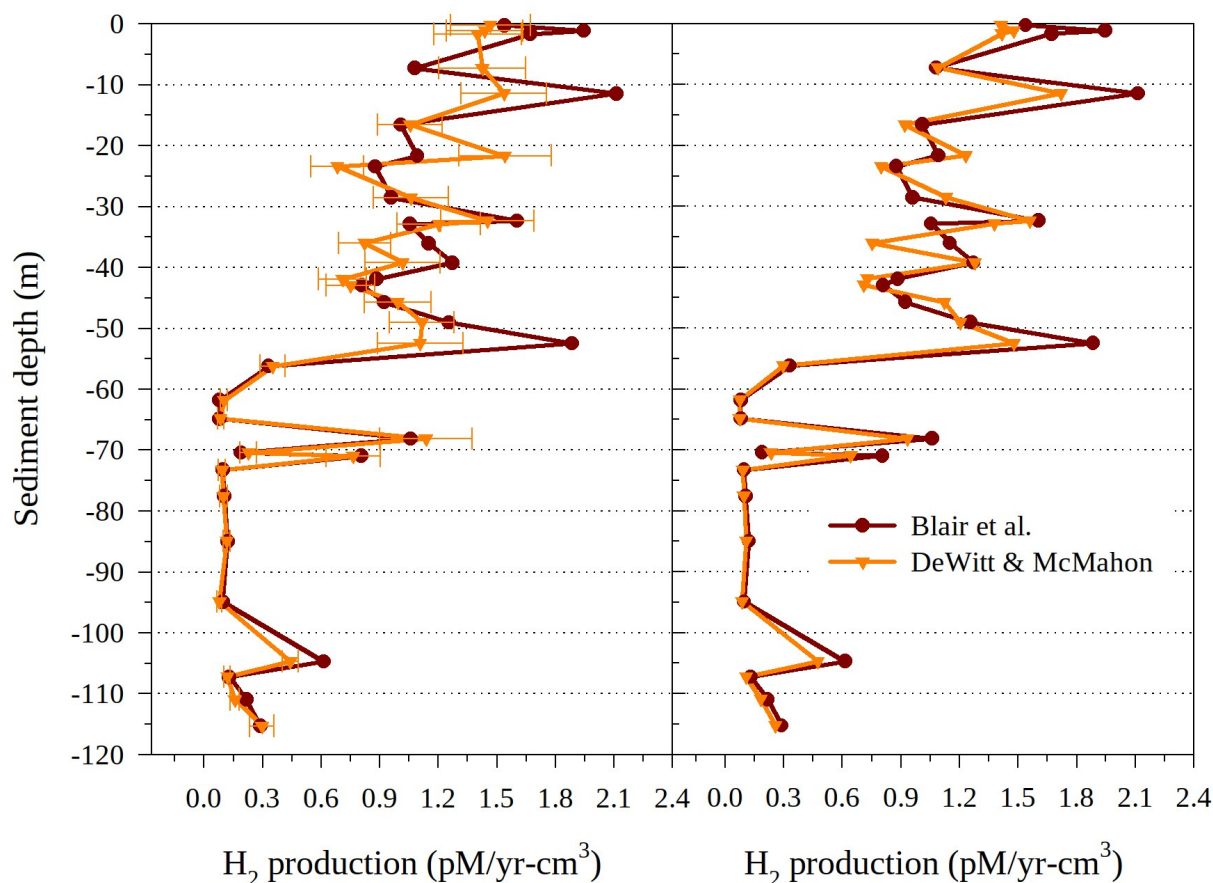
399 In this study, Athy's law is implemented as a multiplicative factor that scales the  
 400 hydrogen production by water radiolysis model of Blair and coworkers (Blair et al., 2007):

401

$$P_{\text{sed}} = P_{\alpha} + P_{\beta} + P_{\gamma} = G_{\alpha}E_{\alpha} + G_{\beta}E_{\beta} + G_{\gamma}E_{\gamma}, \quad (18)$$

402

403 where  $G_{\alpha}$ ,  $G_{\beta}$ , and  $G_{\gamma}$  are the  $\text{H}_2$  yields per unit kinetic energy produced in pure water by  
 404 radiolysis, and  $E_{\alpha}$ ,  $E_{\beta}$ , and  $E_{\gamma}$  are the kinetic energies absorbed by water in bulk rock/sediment  
 405 due to alpha, beta, and gamma decay, respectively. The values of  $G_{\alpha}$ ,  $G_{\beta}$ , and  $G_{\gamma}$  are  $1.57\text{E}4$ ,  
 406  $5.30\text{E}3$ , and  $4.50\text{E}3$  molecules/MeV, respectively (Spinks and Woods, 1990; Blair et al., 2007);  
 407 the values of  $E_{\alpha}$ ,  $E_{\beta}$ , and  $E_{\gamma}$  (in MeV) are determined by the simulation.



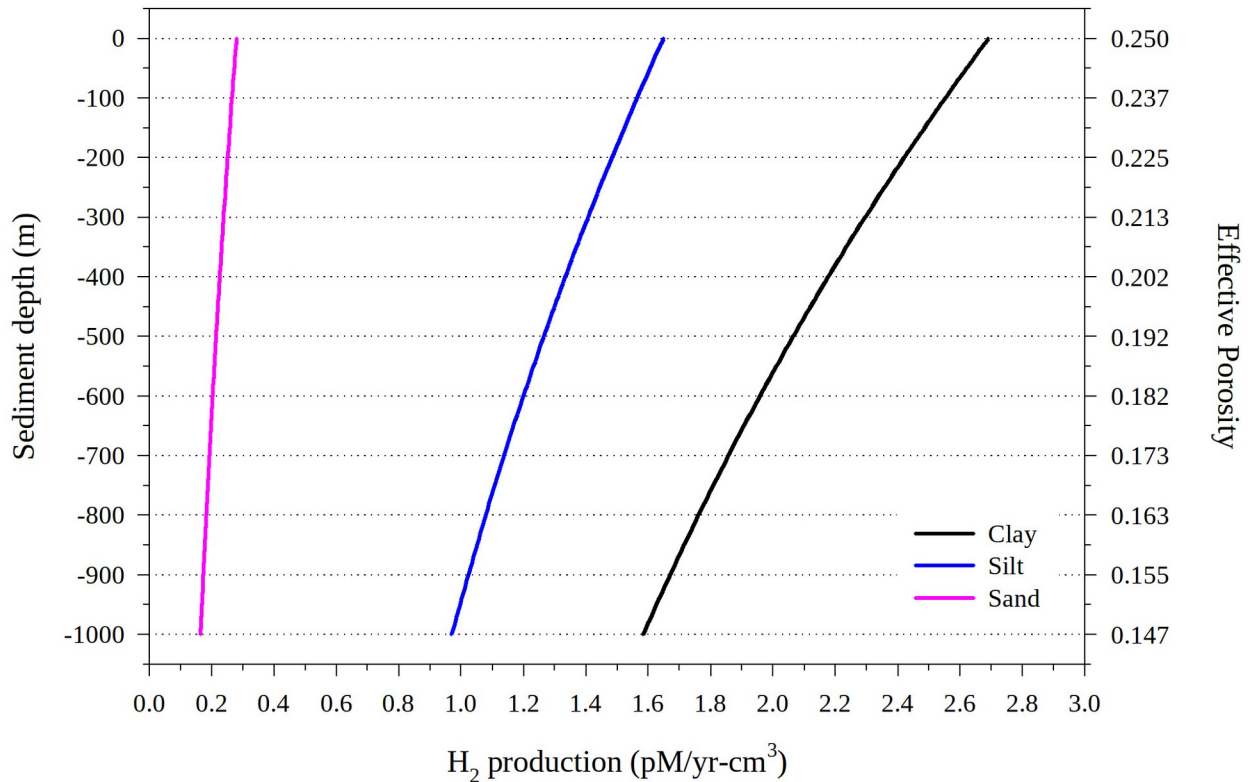
**Figure 3.** A comparison of the predicted radiolytic hydrogen flux using the MC method (orange line) with the analytic model of Blair et al. (2007) using the radionuclide concentrations, grain sizes, and porosities reported for a marine sediment column sampled by the Ocean Drilling Program in the Peru Basin. The left panel shows the anticipated  $H_2$  production after 200 trials, while the right panel shows the same after 200,000 trials. The differences between the predictions of Blair et al. and this study are methodological and do not relate to grain size effects.

Figure 3 compares the predicted  $H_2$  production given by the MC method with those calculated by Blair et al. (2007) from marine sediment column measurements as a function of depth. This figure demonstrates the compatibility of our simulations with the deep marine sediment column in which empirically-determined radionuclide concentrations, grain sizes, and porosities (measured by the Ocean Drilling Program in the Peru Basin) were provided by Blair and coworkers. The left panel in Figure 3 displays a comparison after 200 MC trials, while the right panel shows the same after 200,000 trials. In general, this figure shows that the MC method accurately reproduces the calculations of Blair et al. where confidence is high (i.e., standard error is low); any disagreement above ~55 meters is attributed to 1) the error in measured  $^{232}\text{Th}$  concentrations, and 2) the differing decay energy sums of the two approaches. (Whereas Blair et al. used the endpoint, or maximum, decay energies within a given chain, this study used instead

the average to better represent the spectrum of possible outcomes). Finally, it should be noted that the grain sizes, with an average diameter of 6.2  $\mu\text{m}$  over 120 meters, are too small in this case to attenuate the modelled flux.

### 3. Results

#### 3.1 Effects of Grain Size



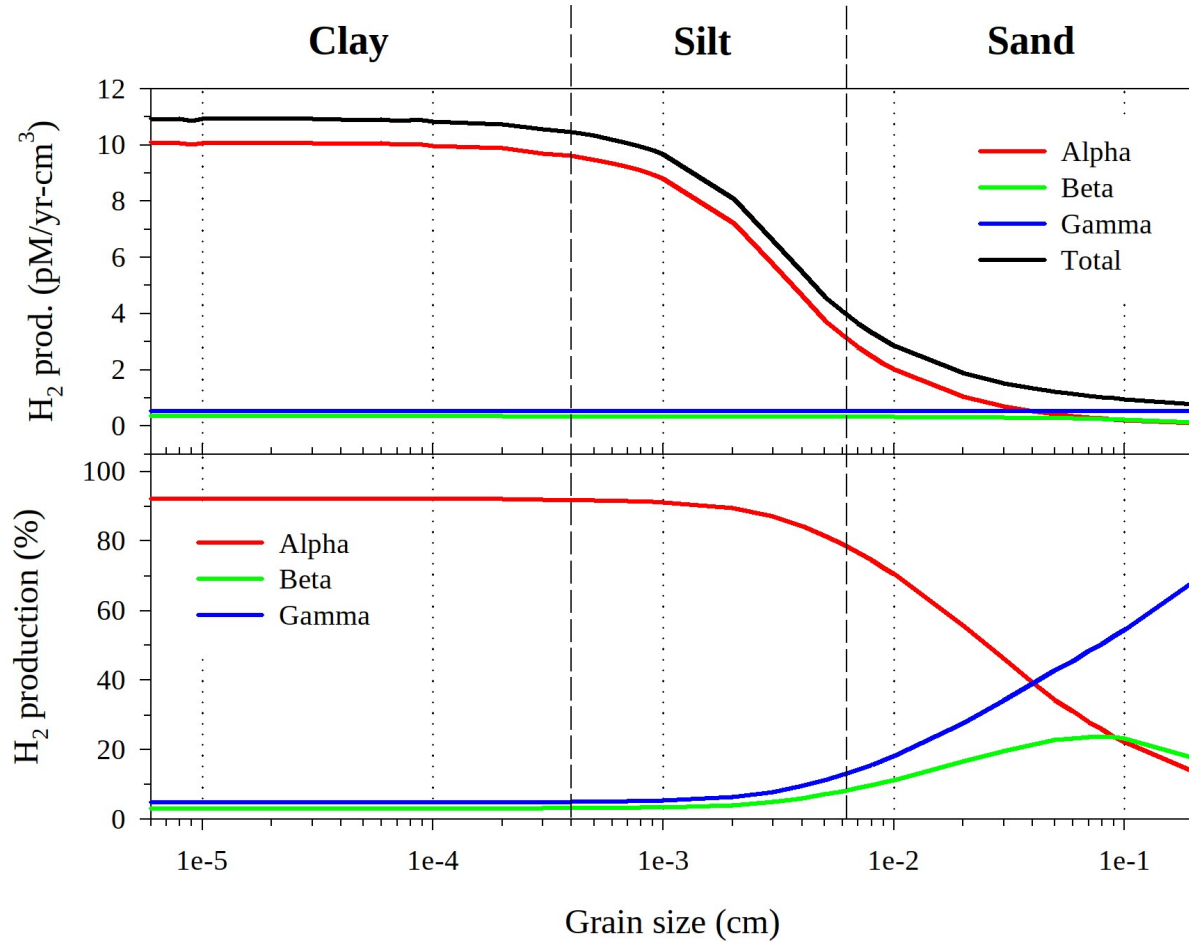
**Figure 4.** Radiolytic hydrogen production as a function of sediment (or rock) depth for the test case of 7.4 ppm U, 2.8 ppm Th, and 1.3% K, with  $\phi_0 = 0.5$  and  $k = 5.3\text{E-}4 \text{ m}^{-1}$ . The  $\text{SiO}_2$  grain size is sampled over clay (0.06 - 3.9  $\mu\text{m}$ ), silt (3.9 - 63  $\mu\text{m}$ ), and sand (63 - 2,000  $\mu\text{m}$ ). (In this simple model, porosity is independent of grain size.)

Figure 4 shows modelled  $\text{H}_2$  production as a function of depth for the test case of 7.4 ppm U, 2.8 ppm Th, and 1.3% K (arbitrary but fairly typical values for geological materials) with  $\phi_0 = 0.5$  and  $k = 5.3\text{E-}4 \text{ m}^{-1}$ ; the grain size is randomly sampled over intervals corresponding to the grain sizes of clay (0.06 - 3.9  $\mu\text{m}$ ), silt (3.9 - 63  $\mu\text{m}$ ), and sand (63 - 2,000  $\mu\text{m}$ ). This figure incorporates the understanding that porosity of rock or sediment column—and therefore overall water content—increases nearer the surface while grain size is independent of depth. In general, these results show that the effect of grain size on  $\text{H}_2$  flux is substantial.



Overall, [Figure 4](#) demonstrates the extent to which radiolytic hydrogen production is larger in smaller grains, and so largest in clay when compared with silt or sand. If alpha radiation is used as a baseline with its comparatively large conversion coefficient ( $G_\alpha$ , [Equation 18](#)), then this can be understood in terms of an average stopping distance that is at least an entire order of magnitude larger than a characteristic clay grain. By contrast,  $H_2$  flux is reduced in silt-sized grains, where characteristic grain sizes are comparable to the average stopping distance of alpha radiation ( $\sim 23 \mu\text{m}$ ). In sand, the production of  $H_2$  is reduced by an entire order of magnitude compared to clay and silt. As before, this phenomenon can be understood in terms of characteristic grain size versus stopping distance and/or attenuation length (in the case of gamma emission). If the average stopping distance of beta radiation from natural radioactive decay is  $\sim 452 \mu\text{m}$ , then there is the possibility that this decay mode—in conjunction with alpha—is also strongly attenuated, thereby allowing the  $H_2$  contribution due to gamma emission to dominate (attenuation length: 3.2 cm or 32,000  $\mu\text{m}$ ).

It is clear from [Figure 4](#) that the decrease in radiolytic hydrogen production as a function of depth is due to Athy's law ([Equation 17](#)). Quantitatively,  $H_2$  fluxes near the surface of 2.7, 1.6, and 0.3  $\text{pM/yr-cm}^3$  in clay, silt, and sand, respectively are reduced to 1.6, 1.0, and 0.2  $\text{pM/yr-cm}^3$  at the maximum depth of 1 km. Moreover, using these values near the surface as a baseline, we can see that the production of  $H_2$  decreases by 41% in clay, silt, and sand at the maximum depth. This reduction depends on the values of  $\phi_0$  and  $k$  in the functional form of Athy's law.



**Figure 5.** Radiolytic hydrogen production via alpha, beta, and gamma decay as a function of  $\text{SiO}_2$  grain size for the test case of 7.4 ppm U, 2.8 ppm Th, and 1.3% K. Top: total  $\text{H}_2$  production per unit volume of water-saturated sediment or rock. Bottom: percentage contribution of each type of radiation to the total  $\text{H}_2$  yield.

Figure 5 compares the effect of grain size on  $\text{H}_2$  production due to alpha, beta, and gamma radiation for the test case presented in Figure 4. (Neither the porosity correction nor the volume correction is applied here since neither would qualitatively alter the comparison.) The top panel shows  $\text{H}_2$  production in units of pico (p, E-12) moles per [Earth] year- $\text{cm}^3$  as a function of  $\text{SiO}_2$  grain radius in cm. Note that  $\text{H}_2$  production due to alpha decay is strongly attenuated as a function of grain size. This phenomenon is explained by the relatively short average stopping distance of alphas ( $\sim 23 \mu\text{m}$  or  $2.3\text{E-}3 \text{ cm}$ ) compared to beta particles (electrons) and gamma rays (photons). Furthermore, this figure also shows that  $\text{H}_2$  production due to alpha decay mirrors the total amount over a logarithmic distribution of grain sizes from clay to sand. This is due to the preponderance of alpha particles in the radioactive emissions of the simulated material, and to the high radiolytic  $\text{H}_2$  yield per unit kinetic energy for alpha particles, which dominates that of beta particles and gamma rays by an entire order of magnitude (Spinks and Woods, 1990).

Figure 5 (bottom) shows  $\text{H}_2$  production in terms of percent fraction as a function of  $\text{SiO}_2$  grain radius in cm. This figure (which would have to be adapted for simulations of materials with

different U, Th and K concentrations) is useful in detailing the relative contributions to  $H_2$  production as a result of alpha, beta, and gamma decay in clay, silt, and sand. In general, [Figure 5](#) suggests that the total  $H_2$  production in this test water-SiO<sub>2</sub> matrix is dominated by the influence of alpha decay. Beta and gamma decay, by contrast, make relatively modest contributions, where little or no attenuation is observed.

In clay,  $H_2$  production from alphas in this simulation is approximately constant at  $10.0 \pm 0.1$  pM/yr-cm<sup>3</sup> where the grain size is smaller than the characteristic, or average, stopping distance as a result of natural radioactive decay. By contrast,  $H_2$  production due to beta and gamma decay is comparatively small, with estimates of  $0.3377 \pm 0.0003$  and  $0.5220 \pm 0.0002$  pM/yr-cm<sup>3</sup>, respectively. This is explained by the differing radiolytic  $H_2$  yields per unit kinetic energy of these radiation types, i.e.,  $G_\alpha$ ,  $G_\beta$ , and  $G_\gamma$  factors. The percent contributions in clay due to alpha, beta, and gamma decay are 92%, 3%, and 5%, respectively. The contribution from alpha decay is thus compatible with Blair et al. (2007), who report an estimate of  $90 \pm 2$  % in the case of clay-like grain sizes and similar radioactivity levels. These simulations also indicate that the main radioisotope contributor in this particular test material is <sup>238</sup>U, with the remaining components of <sup>235</sup>U, <sup>232</sup>Th, and <sup>40</sup>K producing only trace amounts of  $H_2$  irrespective of the decay mode. This figure shows that these percent contributions are roughly constant due to the comparatively weak attenuation of kinetic energy in the small grains characteristic of clay.

The difference in grain size between clay and silt translates into a marked decrease in  $H_2$  yield by the latter. This is not surprising given that a typical alpha particle undergoing radioactive decay in SiO<sub>2</sub> will range on the order of E-3 cm. [Figure 5](#) also shows that the degree of attenuation is substantial: The lower grain-size bound of silt due to alpha decay produces 9.6 pM/yr-cm<sup>3</sup>, while the upper grain-size bound produces 3.2 pM/yr-cm<sup>3</sup>. Similar to clay,  $H_2$  production in silt due to beta and gamma radiation are virtually unchanged due to their comparatively large stopping distance and attenuation length, respectively. The effect of increased grain size is more readily apparent in the percent fractions of  $H_2$  production due to alpha, beta, and gamma decay. At the lower grain-size bound of silt, alpha radiation is responsible for roughly 92% of  $H_2$  production. This reduces to 79% at the upper bound, with the percent fractions of beta and gamma increasing to 8% and 13%, respectively, as a result.

In sand, the attenuation of alpha particles is more pronounced than that observed in silt. (It should be noted that the reduction of  $H_2$  production in this test water-sand matrix qualitatively resembles the escape efficiency of alpha particles seen in [Figure 2](#).) The lower bound of sand due to alpha decay produces 3.2 pM/yr-cm<sup>3</sup>, while the upper bound produces 0.1 pM/yr-cm<sup>3</sup>; between 1 and 2 mm grain size, the production of  $H_2$  due to alpha and beta decay is comparable. The effect of alpha particle attenuation is readily apparent in sand, where the percent fraction contributions of beta and gamma radiation compensate proportionally. At the upper bound (~0.2 cm), alpha, beta, and gamma emissions contribute 14%, 18%, and 68% to  $H_2$  production, respectively. Furthermore, a local maximum in the curve corresponding to beta decay is observed at ~0.08 cm, suggesting that beta particles “range-out” in grain sizes characteristic of sand. This is consistent with the average beta-particle stopping distance of ~0.05 cm in natural radioactive decay (National Institute of Standards and Technology, 2021b). No such maximum is observed in the curve corresponding to gamma radiation, however, owing to the comparatively large average attenuation length (~3.2 cm) of this decay mode in rock/sediment, not to mention the differing physics of photon propagation in matter. Given the grain sizes explored in this study, we have naturally found that all gamma radiation escapes from the originating grain.

531

532 

### 3.2 Application to Natural Systems

533 Having validated our method for predicting the radiolytic hydrogen flux in clay, silt, and  
 534 sand, in this section we consider how grain size could affect radiolytic yields from a variety of  
 535 geologically interesting natural materials of known (or estimable) porosity and radionuclide  
 536 concentration. [Table 2](#) summarizes the values of key parameters (other than grain size) used here  
 537 to simulate porewater radiolysis at Jezero Crater on Mars, the average upper continental crust of  
 538 the Earth, monazite beach sand found in Ullal (India), the upper half of the Peru Basin sediment  
 539 column examined in [Figure 3](#), and Upper Vredefort Crust of South Africa.

540

541 **Table 2.** A summary of the input parameters used to generate Figures [6-10](#). The activities are  
 542 computed using [Equation 16](#) with a mass density of 2.7 g/cm<sup>3</sup>. The total activity per unit volume  
 543 of rock/sediment  $A_{\text{tot}}$  is the sum of all radioisotope contributions. We assume that hard,  
 544 crystalline rocks have depth-invariant porosity since they are effectively incompressible over the  
 545 depth range sampled (Gleeson et al., 2016). For the other geological settings, we set  $k$ , the  
 546 compaction coefficient, to 5.3E-4 m<sup>-1</sup> on Earth and 3.54 m<sup>-1</sup> on Mars (Clifford et al. 2010).

547

| Geological Formation                      | $A_{\text{tot}}$<br>(Bq/cm <sup>3</sup> ) | $A_{40\text{-K}}$<br>(%) | $A_{232\text{-Th}}$<br>(%) | $A_{235\text{-U}}$<br>(%) | $A_{238\text{-U}}$<br>(%) | $\phi_0$<br>(%) | $k$ (m <sup>-1</sup> ) | Reference   |
|---|---|--------------------------|----------------------------|---------------------------|---------------------------|-----------------|------------------------|---|
| Jezero Crater, Mars                       | 0.3                                       | ~96                      | $\gtrsim 2$                | $\ll 1$                   | $\lesssim 2$              | 35              | 3.546<br>1E-4          | Dzaugis et al. (2018)<br>Clifford et al. (2010) for $k$ |
| Upper continental crust (Earth, granitic) | 2.2                                       | ~90                      | $\gtrsim 5$                | $< 1$                     | $\gtrsim 4$               | 1               | 0                      | Aquilina et al. (2004)                                  |
| Monazite beach sediment, Ullal, India     | 6.4                                       | ~7                       | ~77                        | $< 1$                     | $\gtrsim 15$              | 40              | 5.3E-4                 | Radhakrishna et al. (1993) except $\phi_0$              |
| Peru Basin sediment column                | 2.3                                       | ~86                      | $\gtrsim 7$                | $< 1$                     | $\gtrsim 6$               | 88              | 5.3E-4                 | Blair et al. (2007)                                     |
| Upper Vredefort Crust                     | 3.3                                       | ~92                      | $\gtrsim 5$                | $< 1$                     | $\gtrsim 2$               | 0.2<br>5        | 0                      | Lin et al. (2005)                                       |

548

The factor  $A_{\text{tot}}$  (decay/sec-cm<sup>3</sup>) listed in [Table 2](#) is used in part to convert the H<sub>2</sub> production of [Equation 18](#) (molecules H<sub>2</sub> / decay) to units of M/yr-cm<sup>3</sup>. The other activities listed in this table serve as “probability selectors” for the Monte Carlo simulation. (For example, the radioisotope <sup>40</sup>K, being relatively abundant in minerals, is commonly selected by the random number generator.) The parameters  $\phi_0$  and  $k$  (surface porosity and compaction coefficient, respectively) are used in Athy’s law ([Equation 17](#)) to determine the effective sediment porosity as a function of depth. For the upper half of the Peru Basin sediment column, we used the average of the porosity measurements above ~55 meters to extrapolate this geological formation to greater depths.

Similar to [Figure 4](#), [Figure 6](#) shows modelled H<sub>2</sub> production as a function of sediment/rock depth for Jezero Crater on Mars, the upper continental crust of the Earth, monazite beach sediment found in Ullal (India), the upper half of the Peru Basin sediment column examined in [Figure 3](#), and Upper Vredefort Crust of South Africa. As before, the grain size is randomly sampled over intervals corresponding to clay (0.06 - 3.9  $\mu\text{m}$ ), silt (3.9 - 63  $\mu\text{m}$ ), and sand (63 - 2,000  $\mu\text{m}$ ).

Regardless of grain size, [Figure 6](#) demonstrates that radiolytic hydrogen flux is highest in the monazite beach sediment of Ullal, India, and lowest in Upper Vredefort Crust of South Africa, when nearest-neighbor effects in the form of porosity are considered. The observed disparity between high and low is three orders of magnitude across clay, silt, and sand; the ordering of these depth-flux curves appears to arise from a complex interplay of the factors given in [Table 2](#).

The effects of grain size on mineral radioactivity and radiolysis at a given depth can be quantified by making a straightforward comparison of H<sub>2</sub> flux values at any depth (n.b., Athy’s law). Choosing values near the surface and the grain sizes of silt and sand—where characteristic grain sizes attenuate alpha radiation—the ratio of relative change sand:silt reveals a factor of  $2.30 \pm 0.03$  for the upper continental crust of the Earth, the upper half of the Peru Basin sediment column, and Upper Vredefort Crust. (As a means of shorthand, we will refer to these geological formations collectively as the “typical Earth group”.) That is, H<sub>2</sub> production is reduced consistently by about  $\frac{3}{7}$  across geological formations of similar radioactivity when comparing silt versus sand at a given depth. For the case of Jezero Crater on Mars, this factor is comparable, or 2.21. However, the unusual radioactive conditions found in the monazite beach sand of Ullal, India produce a silt/sand “shifting” factor of 2.48, or about 7% more than elsewhere. Furthermore, it should be noted that the combination of  $\phi_0$  and  $k$  on Mars result in a reduction of H<sub>2</sub> production by 30% in all grain sizes at the maximum depth, which is lower than 41% in the case of terrestrial conditions. In other words, the slopes of the depth-flux curves, when viewed in semi-log space, are steeper.

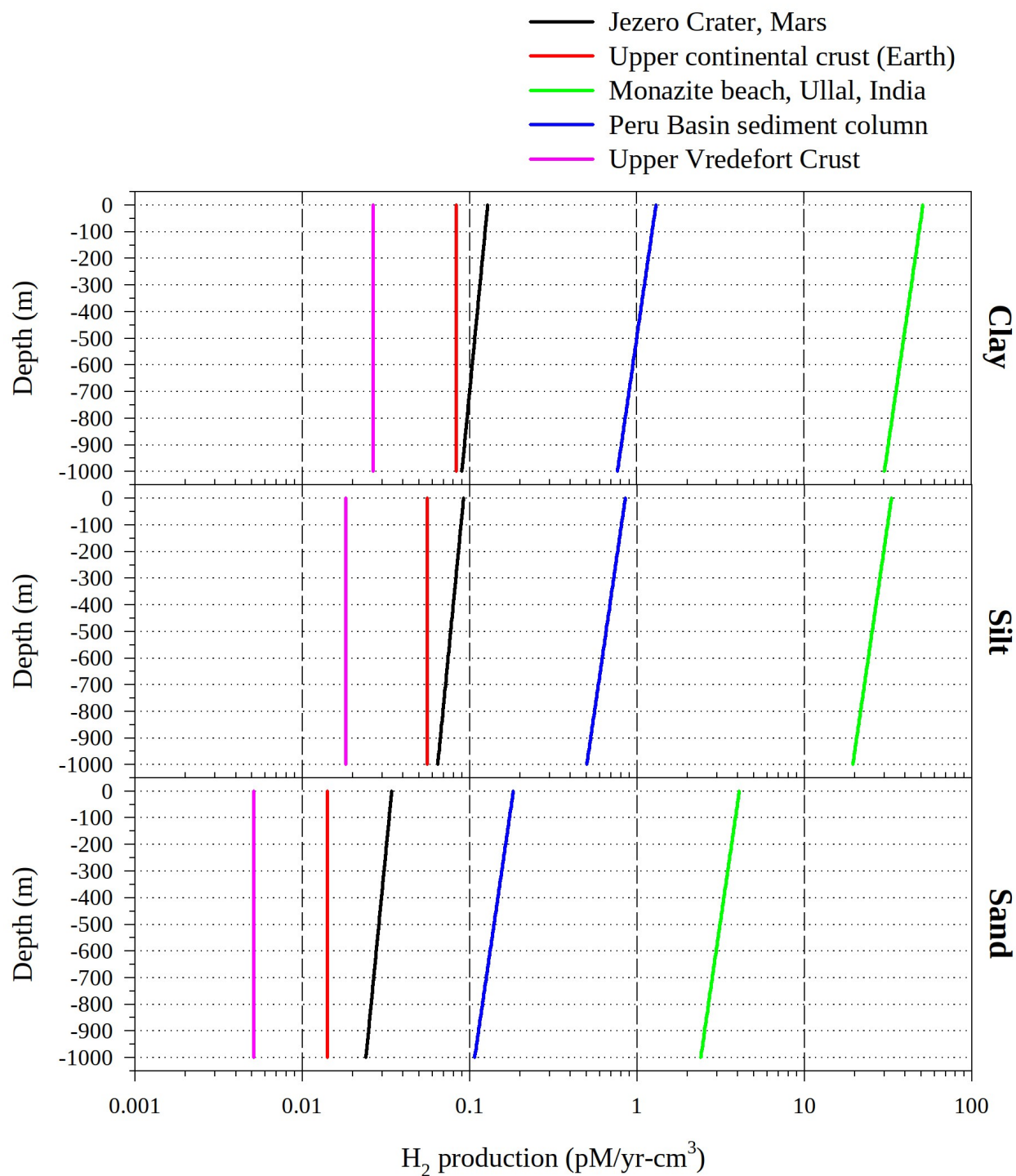


**Figure 6.** Radiolytic hydrogen production as a function of depth in a variety of geological settings. The  $SiO_2$  grain size is sampled over clay (0.06 - 3.9  $\mu m$ ), silt (3.9 - 63  $\mu m$ ), and sand (63 - 2,000  $\mu m$ ).

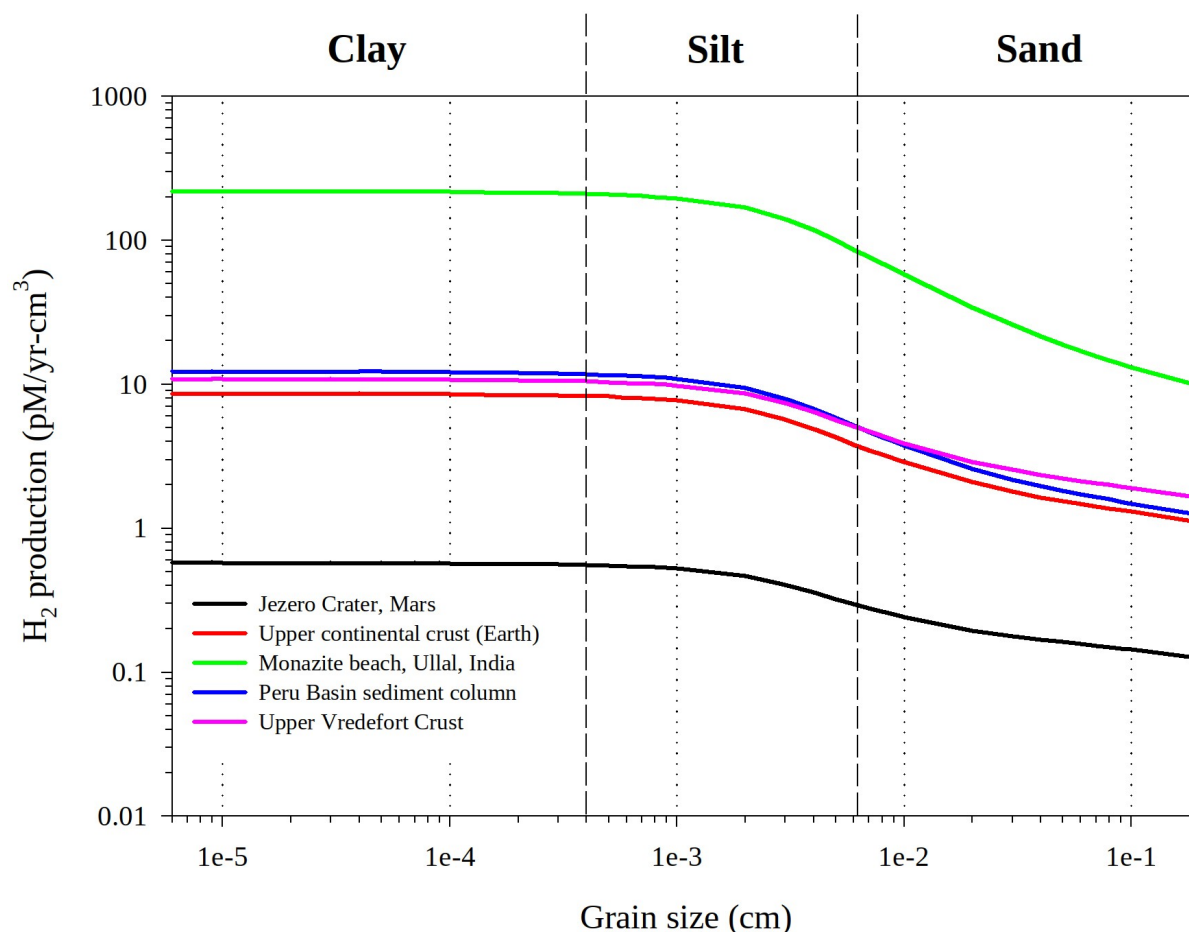


**Figure 7.** Total radiolytic hydrogen production (from **all sources**) as a function of SiO<sub>2</sub> grain size in a variety of geological formations.

Figure 7 shows total H<sub>2</sub> production in units of pico (p, E-12) moles per [Earth] year-cm<sup>3</sup> as a function of SiO<sub>2</sub> grain radius in cm for the geological formations presented in Figure 6. This figure shows that the monazite beach sand of Ullal, India produces an H<sub>2</sub> flux that is three orders of magnitude larger than Jezero Crater on Mars. Consistent with the observation in Figure 6, the typical Earth group predicts comparable fluxes of radiolytic hydrogen owing to their similar overall radioactivity. If monazite beach sand were reduced to a grain size in the range of clay, H<sub>2</sub> production from all sources of radiation would be approximately  $216 \pm 2$  pM/yr-cm<sup>3</sup> (compared to 86 and 10 pM/yr-cm<sup>3</sup> at the upper bounds of silt and sand, respectively). This comparatively large H<sub>2</sub> flux stands in contrast to the typical Earth group, which displays an average of  $10.5 \pm 1.8$  pM/yr-cm<sup>3</sup>. At the lower end, Jezero Crater on Mars gives an estimate of  $0.57 \pm 0.01$  pM/yr-cm<sup>3</sup>. At the grain size of silt, the typical Earth group gives a reduced H<sub>2</sub> flux of  $4.7 \pm 0.8$  pM/yr-cm<sup>3</sup> where grain sizes approach those characterizing sand (i.e., the upper bound of silt). Similarly, Jezero Crater reduces to 0.3 pM/yr-cm<sup>3</sup>. The slope of the decline in H<sub>2</sub> flux with increasing grain size becomes shallower in sand. Specifically, at ~0.2 cm, radiolytic hydrogen production in the typical Earth group and Jezero Crater is reduced to  $1.3 \pm 0.3$  and 0.1 pM/yr-cm<sup>3</sup>, respectively. Finally, since neither the porosity correction nor the volume correction is

applied here, the reader should note that the ordering from highest to lowest in [Figure 7](#) naturally differs from that of [Figure 6](#).

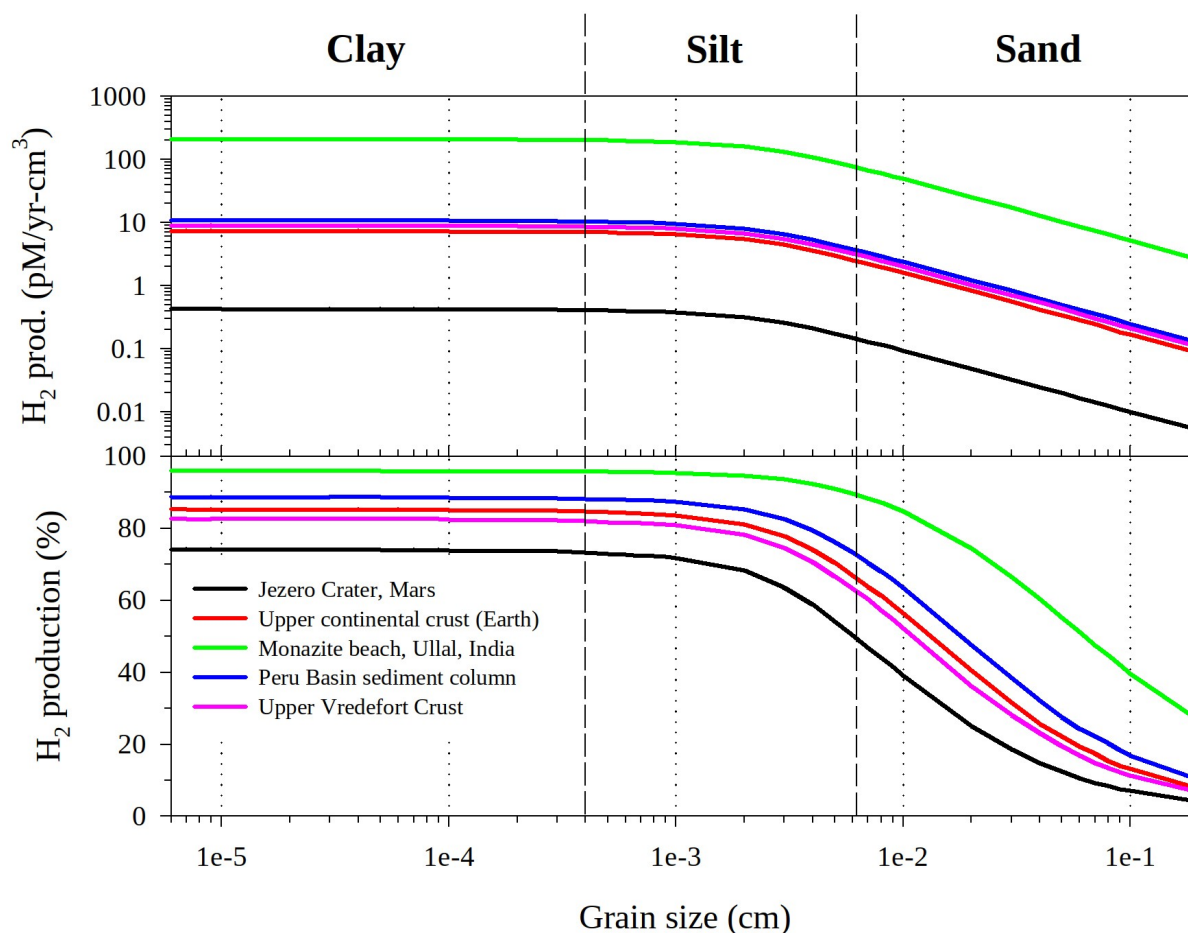


**Figure 8.** Radiolytic hydrogen production due to **alpha** decay as a function of SiO<sub>2</sub> grain size in a variety of geological formations.

[Figure 8](#) (top) shows H<sub>2</sub> production due to alpha decay in units of pico (p, E-12) moles per [Earth] year-cm<sup>3</sup> as a function of SiO<sub>2</sub> grain radius in cm for a variety of geological formations. With regard to alpha decay only, the output from the MC simulations shows that the monazite beach sand of Ullal, India produces the highest H<sub>2</sub> flux overall, while Jezero Crater on Mars produces the lowest; this finding is consistent across all grain sizes. Furthermore, because of their comparable concentrations of thorium and uranium—which decay largely via alpha emission—the typical Earth group produces similar amounts of H<sub>2</sub> across all grain sizes. Beyond these general observations, [Figure 8](#) is consistent with [Figure 5](#) regarding the attenuation of alpha radiation as compared to beta ([Figure 9](#)) and gamma ([Figure 10](#)). [Figure 8](#) (bottom) shows H<sub>2</sub> production in terms of percent fraction as a function of SiO<sub>2</sub> grain radius in cm.



When only alpha radiation is considered, our simulations predict that radiolytic hydrogen production would be  $\sim 207 \pm 2$  pM/yr-cm<sup>3</sup> if monazite beach sand were reduced to a grain size in the range of clay. The typical Earth group displays a middle ground of H<sub>2</sub> flux due to alpha decay, with an average of  $8.9 \pm 1.7$  pM/yr-cm<sup>3</sup> in clay. As noted before, this is due to their similar concentrations of thorium and uranium. Jezero Crater is expected to produce a flux that is an order of magnitude below the typical Earth group, with an estimate of  $0.42 \pm 0.01$  pM/yr-cm<sup>3</sup>. From the standpoint of alpha decay, our simulations show (in descending order)  $95.81 \pm 0.04$  % (if reduced to clay),  $88.5 \pm 0.1$  %,  $85.1 \pm 0.2$  %, and  $82.5 \pm 0.2$  % for monazite beach sediment, the Peru Basin sediment column, the average of the upper continental crust of the Earth, and Upper Vredefort Crust, respectively, with an average of  $85.4 \pm 3.0$  % for the typical Earth group. This is explained by the <sup>232</sup>Th and <sup>238</sup>U parameters of [Table 2](#), which are derived from the source thorium and uranium measurements of previous studies. (The result for Jezero Crater is slightly lower at  $73.9 \pm 0.3$  % for the same reason.)

All geological settings studied here attenuate in a predictable manner in silt-sized grains, with estimates of 76.9,  $3.2 \pm 0.6$ , and  $0.1$  pM/yr-cm<sup>3</sup> for monazite beach sand (if appropriately reduced in grain size), the typical Earth group, and Jezero Crater, respectively. Similar to [Figure 5](#) (bottom), in silt the effect of increased grain size is visible on the percent fraction of H<sub>2</sub> production due to alpha decay. This is explained by the tendency of alpha particles to range-out in grain sizes comparable to the characteristic stopping distance of natural radioactive decay. The similar shapes of the curves observed in the typical Earth group are due to their analogous radioactive composition; at the upper bound of silt, the percent contribution from alpha decay is reduced to  $67.7 \pm 5.0$  %. Bookending the typical Earth group are size-adjusted monazite beach sediment and Jezero Crater, which are reduced to 89.6% and 50.1%, respectively.

In grain sizes characteristic of sand, [Figure 8](#) shows that H<sub>2</sub> production due to alpha decay is reduced substantially: At  $\sim 0.2$  cm, this figure gives estimates of 2.59,  $0.11 \pm 0.02$ , and  $0.005$  pM/yr-cm<sup>3</sup> for monazite beach sand, the typical Earth group, and Jezero Crater, respectively. Similar to [Figure 5](#) (bottom), alpha emissions from natural radioactive decay are further attenuated in sand. At the upper bound ( $\sim 0.2$  cm), alpha emission contributes 26.5%,  $8.2 \pm 1.8$  %, and 4.2% to H<sub>2</sub> production in monazite beach sand, the typical Earth group, and Jezero Crater, respectively. As noted in [Figure 5](#), the upper bound of sand in [Figure 8](#) displays a tapering effect that is consistent with the escape efficiency of alpha particles seen in [Figure 2](#).

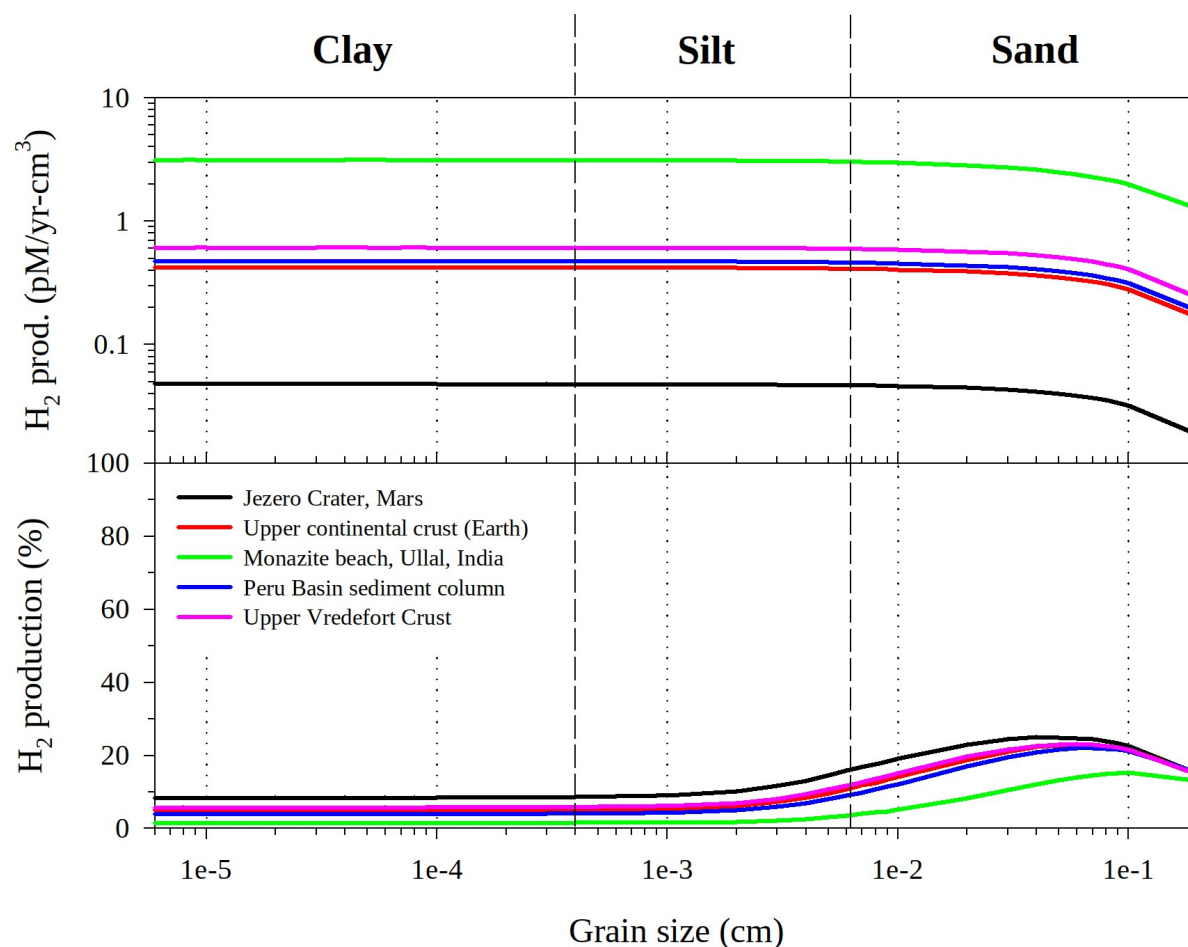


**Figure 9.** Radiolytic hydrogen production due to **beta** decay as a function of  $\text{SiO}_2$  grain size in a variety of geological formations.

Figure 9 (top) shows  $\text{H}_2$  production due to beta decay in units of pico (p, E-12) moles per [Earth] year- $\text{cm}^3$  as a function of  $\text{SiO}_2$  grain radius in cm for a variety of geological formations. In contrast to Figure 8, where the attenuation of alpha particles is observed in silt, in Figure 9 this same phenomenon occurs in grain sizes that characterize sand. This is explained by the substantially larger stopping distance of beta particles that are routinely emitted via natural radioactive decay ( $\sim 0.05$  cm). Similar to Figure 8, this figure also shows that—across all grain sizes—the monazite beach sand of Ullal, India produces the most  $\text{H}_2$  overall, a finding that is one order of magnitude above the typical Earth group. Figure 9 (bottom) shows  $\text{H}_2$  production in terms of percent fraction as a function of  $\text{SiO}_2$  grain radius in cm. Here a local maximum in sand is observed for all geological units.

If monazite beach sand were reduced to a grain size in the range of clay, our simulations predict that radiolytic hydrogen production would be approximately constant at  $3.122 \pm 0.002$   $\text{pM/yr-cm}^3$ . In clay the typical Earth group displays an  $\text{H}_2$  flux due to beta decay that is one order of magnitude smaller:  $0.5 \pm 0.1$   $\text{pM/yr-cm}^3$ . Jezero Crater on Mars is expected to produce a flux that is an order of magnitude below the typical Earth group, with an estimate of  $0.04776 \pm 0.00003$   $\text{pM/yr-cm}^3$ . In descending order, our simulations show percent fraction contributions

due to beta decay of  $8.37 \pm 0.08$  %,  $4.84 \pm 0.9$  %, and  $1.45 \pm 0.01$  % for Jezero Crater, the typical Earth group, and monazite beach sand (in the form of clay), respectively. Similar to [Figure 8](#), these results are explained by the  $^{40}\text{K}$  parameters of [Table 2](#), where potassium decays the most frequently via beta emission.

[Figure 9](#) shows that monazite beach sand, if reduced to grain sizes characteristic of silt, is predicted to produce an  $\text{H}_2$  flux due to beta emission that is only slightly diminished compared to that in clay, or  $3.0 \text{ pM/yr-cm}^3$  at the upper bound. What is more, the typical Earth group shows almost no variation both qualitatively and quantitatively (at  $\sim 0.006 \text{ cm}$ :  $0.5 \pm 0.1 \text{ pM/yr-cm}^3$ ). This is also observed in the case of Jezero Crater, or  $0.04685 \text{ pM/yr-cm}^3$  at the upper bound of silt. Examining [Figure 9](#) (bottom), if monazite beach sand were reduced to silt, the percent contribution due to beta decay would increase marginally to 3.5% at the upper bound. Furthermore, Jezero Crater and the typical Earth group also increase to 15.8% and  $10.5 \pm 1.4$  %, respectively. Comparing these results to [Figure 8](#) (bottom), we can understand this phenomenon in terms of the tendency of alpha particles to range-out in silt (i.e., beta compensates proportionally).

In grain sizes characteristic of sand, where beta particles from natural radioactive decay have the tendency to range-out,  $\text{H}_2$  production is reduced. Specifically, at the upper bound ( $\sim 0.2 \text{ cm}$ ), [Figure 9](#) (top) gives estimates of 1.27,  $0.20 \pm 0.04$ , and  $0.02 \text{ pM/yr-cm}^3$  for monazite beach sand, the typical Earth group, and Jezero Crater, respectively. Beta emissions are substantially attenuated in sand where the characteristic range of these particles ( $\sim 0.05 \text{ cm}$ ) is comparable to the grain size. That is, beta particles range-out in sand in much the same way as alpha particles in silt. Moreover, it can be seen from [Figure 9](#) that the peak contribution from beta emission occurs at about 0.04, 0.06, and 0.1 cm for Jezero Crater, the typical Earth group, and monazite beach sand, respectively.

[Figure 10](#) shows  $\text{H}_2$  production due to gamma decay in units of pico (p, E-12) moles per [Earth]  $\text{year-cm}^3$  as a function of  $\text{SiO}_2$  grain radius in cm for a variety of geological formations. In contrast to alpha and beta emission, no attenuation is observed in radiolytic hydrogen production as a function of grain size. This is explained by 1) the differing physics of photon interaction with matter, and 2) the large attenuation length ( $\sim 3.2 \text{ cm}$ ) characteristic of gamma decay in a natural setting. Similar to [Figure 9](#) (bottom), this figure shows that Jezero Crater produces the most  $\text{H}_2$  across all grain sizes due to gamma decay, while monazite beach sand produces the least, with the typical Earth group presenting a middle ground. These results are sensible given the  $^{40}\text{K}$  parameters of [Table 2](#), which suggest the frequent emission of a residual gamma ray as radioactive potassium decays to  $^{40}\text{Ar}$ .

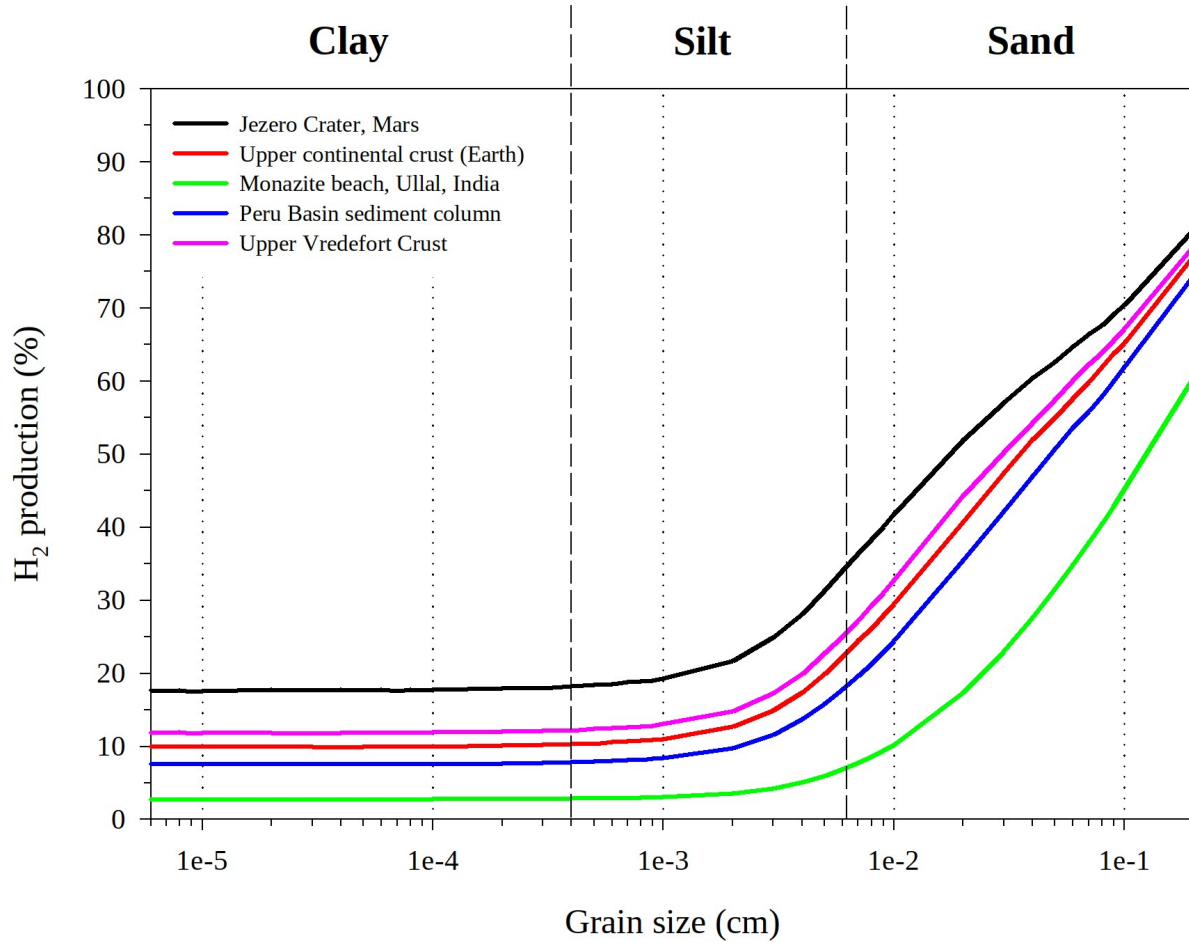


**Figure 10.** Radiolytic hydrogen production due to gamma decay as a function of SiO<sub>2</sub> grain size in a variety of geological formations.

Gamma rays are photons that lack charge and mass. Consequently they are not subject to electromagnetic slowing as in the case of alpha and beta particles. Thus, the H<sub>2</sub> contribution of gamma rays is constant where the grain size is much less than the characteristic attenuation length found in natural radioactive decay. Our simulations confirm this phenomenon with a summary in [Table 3](#).

**Table 3.** Average H<sub>2</sub> production in units of pM/yr-cm<sup>3</sup> due to gamma decay for a variety of geological settings predicted using the parameters given in Table 2.

|         | Jezero Crater, Mars | Upper continental crust (Earth) | Monazite beach sediment, Ullal, India | Peru Basin sediment column | Upper Vredefort Crust |
|---------|---------------------|---------------------------------|---------------------------------------|----------------------------|-----------------------|
| Average | 0.10122             | 0.8509                          | 5.928                                 | 0.9185                     | 1.278                 |

|                    |         |        |       |        |       |
|--------------------|---------|--------|-------|--------|-------|
| Standard Deviation | 0.00004 | 0.0004 | 0.002 | 0.0004 | 0.001 |
|--------------------|---------|--------|-------|--------|-------|

In clay (0.06 - 4  $\mu\text{m}$ ), [Figure 10](#) shows percent fraction contributions due to gamma decay of  $17.7 \pm 0.2 \%$ ,  $9.8 \pm 2.2 \%$ , and  $2.74 \pm 0.03 \%$  for Jezero Crater, the typical Earth group, and monazite beach sand (size-reduced), respectively, in descending order. As noted in [Figure 9](#) (bottom), the sequencing observed here is attributed to the relative radioactivity of these geological formations.

In silt (5 - 60  $\mu\text{m}$ ), this figure shows that Jezero Crater, the typical Earth group, and monazite beach sand (reduced in size to silt) increase to 34.1%,  $21.8 \pm 3.6 \%$ , and 6.9%, respectively. As noted previously, this is a further consequence of the tendency of alpha particles to range-out in silt, where beta ([Figure 9](#), bottom) and gamma ([Figure 10](#)) compensate proportionally.

In sand (70 - 2,000  $\mu\text{m}$ ), alpha and beta particles are shown to have a diminished effect on the percent contribution to  $\text{H}_2$  production. At this point gamma emission dominates radiolytic hydrogen production to the extent that Jezero Crater, the typical Earth group, and monazite beach sand contribute 80.9%,  $76.8 \pm 2.0 \%$ , and 60.6%, respectively, at the upper bound. Gamma rays characteristic of natural radioactive decay are expected to attenuate in grain sizes of between one and two orders of magnitude beyond those of sand.

#### 4. Discussion and Conclusions

This study has developed and validated a Monte Carlo method that simulates the physics of mineral radiation in order to predict the production of  $\text{H}_2$  as a function of mineral grain size and radioisotope composition. The results given here confirm that grain size is a major control on overall radioactivity, and consequently, on radiolytic  $\text{H}_2$  yield. The dominant mode of decay (i.e., as controlled by the radioisotope composition) also tends to influence the degree to which  $\text{H}_2$  flux is attenuated as a function of grain size; materials whose radioactivity is dominated by their potassium content will show a less severe attenuation of  $\text{H}_2$  flux with increasing grain size since  $^{40}\text{K}$  radiation is dominated by beta rather than alpha emissions. When our method is applied to a generic test case, the standard geological classification of grain sizes seems to suggest that clay can produce up to an order of magnitude more  $\text{H}_2$  per unit time than sand. Furthermore, we have used the physics encoded in our simulation method to confirm that alpha particles range-out in silt, while beta particles range-out in grain sizes characteristic of sand. Additionally, all gamma rays, by virtue of their attenuation length, were found to escape to the surrounding water layer in our simulations, with the result that gamma radiation dominates  $\text{H}_2$  production for grain sizes larger than sand. Consequently, we do not expect gamma radiation to attenuate until grain sizes exceed those of sand by at least one order of magnitude.

We have applied our numerical method to a variety of interesting natural systems as a means of exploring the magnitude of porewater radiolysis. This exploration was conducted using compositional data from real geological units in order to demonstrate the dependence of natural radionuclide concentration and bulk porosity on radiolytic hydrogen flux. A survey of our simulation results seems to suggest that  $\text{H}_2$  production in these geological units is modulated by

alpha decay in rock/sediment grain sizes characteristic of clay and silt, while beta and gamma emissions take over as a secondary control in sand-sized grains.

These results were obtained for spherical grains. In real rocks and sediments, grains of a size likely to attenuate alpha radiation considerably (e.g., sand) are likely to be fairly spherical and equant, whereas highly non-spherical grains (e.g., platy clay crystals) are likely to be small and thus minimally attenuating. It follows that our general results may be fairly realistic for complex geological materials. Nevertheless, our Monte Carlo method can be readily adapted for materials with constituent grains of arbitrary size and shape, of any composition, on any planetary body. As a consequence, it should now be possible to estimate more accurately how radiolytic hydrogen might contribute to the habitability of microbial life in porous materials on Earth, Mars, and beyond.

## Acknowledgments and Data

The authors greatly appreciate the helpful discussions with Eric Benton at Oklahoma State University and Regina DeWitt at East Carolina University. S.M. also thanks Barry B. McMahon for helpful discussions about the geometry in [Supplementary Information S2](#).

## References

- Aitken, M. J. (1985). *Thermoluminescence Dating*. Orlando: Academic Press.
- Aquilina, L., de Dreuz, J. R., Bour, O., & Davy, P. (2004). Porosity and fluid velocities in the upper continental crust (2 to 4 km) inferred from injection tests at the Soultz-sous-Forêts geothermal site. *Geochimica et Cosmochimica Acta*, 68(11), 2405-2415.
- Bethe, H. (1930). Zur theorie des durchgangs schneller korpuskularstrahlen durch materie. *Annalen der Physik*, 397(3), 325-400.
- Bethe, H., & Heitler, W. (1934). On the stopping of fast particles and on the creation of positive electrons. *Proceedings of the Royal Society of London. Series A, Containing Papers of a Mathematical and Physical Character*, 146(856), 83-112.
- Blair, C. C., D'Hondt, S., Spivack, A. J., & Kingsley, R. H. (2007). Radiolytic hydrogen and microbial respiration in subsurface sediments. *Astrobiology*, 7(6), 951-970.
- Brookhaven National Laboratory (2021). Interactive Chart of Nuclides (2021), <http://www.nndc.bnl.gov/nudat2>
- Bouquet, A., Glein, C. R., Wyrick, D., & Waite, J. H. (2017). Alternative energy: production of H<sub>2</sub> by radiolysis of water in the rocky cores of icy bodies. *The Astrophysical Journal Letters*, 840(1), L8.
- Chapelle, F. H., O'Neill, K., Bradley, P. M., Methé, B. A., Ciufo, S. A., Knobel, L. L., & Lovley, D. R. (2002). A hydrogen-based subsurface microbial community dominated by methanogens. *Nature*, 415(6869), 312-315.

- 808 Clifford, S. M., Lasue, J., Heggy, E., Boisson, J., McGovern, P., & Max, M. D. (2010). Depth of  
809 the Martian cryosphere: Revised estimates and implications for the existence and detection of  
810 subpermafrost groundwater. *Journal of Geophysical Research: Planets*, 115(E7).
- 811 Dzaugis, M. E., Spivack, A. J., Dunlea, A. G., Murray, R. W., & D'Hondt, S. (2016). Radiolytic  
812 hydrogen production in the subseafloor basaltic aquifer. *Frontiers in microbiology*, 7, 76.
- 813 Dzaugis, M., Spivack, A. J., & D'Hondt, S. (2018). Radiolytic H<sub>2</sub> production in martian  
814 environments. *Astrobiology*, 18(9), 1137-1146.
- 815 Einstein, A. (1905). Über einen die Erzeugung und Verwandlung des Lichtes betreffenden  
816 heuristischen Gesichtspunkt *Annalen der Physik* 17, 132.
- 817 Fermi, E. (1940). The ionization loss of energy in gases and in condensed materials. *Physical*  
818 *Review*, 57(6), 485.
- 819 Fowler, A. C., & Yang, X. S. (1998). Fast and slow compaction in sedimentary basins. *SIAM*  
820 *Journal on Applied Mathematics*, 59(1), 365-385.
- 821 Freund, F., Dickinson, J. T., & Cash, M. (2002). Hydrogen in rocks: an energy source for deep  
822 microbial communities. *Astrobiology*, 2(1), 83-92.
- 823 Gleeson, T., Befus, K. M., Jasechko, S., Luijendijk, E., & Cardenas, M. B. (2016). The global  
824 volume and distribution of modern groundwater. *Nature Geoscience*, 9(2), 161-167.
- 825 Gould, R. J., & Schréder, G. P. (1967). Pair production in photon-photon collisions. *Physical*  
826 *Review*, 155(5), 1404.
- 827 Hofmann, B.A. (1992). Isolated reduction phenomena in red beds: a result of porewater  
828 radiolysis. In Y.K. Kharaka, and A.S. Maest (Eds.), *Water–Rock Interaction* (pp 503–506).  
829 Rotterdam: A.A. Balkema.
- 830 Klein, O., & Nishina, Y. (1929). Über die Streuung von Strahlung durch freie Elektronen nach  
831 der neuen relativistischen Quantendynamik von Dirac. *Zeitschrift für Physik*, 52(11), 853-868.
- 832 Kral, T. A., Brink, K. M., Miller, S. L., & McKay, C. P. (1998). Hydrogen consumption by  
833 methanogens on the early Earth. *Origins of Life and Evolution of the Biosphere*, 28(3), 311-319.
- 834 Krumholz, L. R., McKinley, J. P., Ulrich, G. A., & Suflita, J. M. (1997). Confined subsurface  
835 microbial communities in Cretaceous rock. *Nature*, 386(6620), 64-66.
- 836 Lefticariu, L., Pratt, L. A., LaVerne, J. A., & Schimmelmann, A. (2010). Anoxic pyrite oxidation  
837 by water radiolysis products—a potential source of biosustaining energy. *Earth and Planetary*  
838 *Science Letters*, 292(1-2), 57-67.
- 839 Lin, L. H., Hall, J., Lippmann-Pipke, J., Ward, J. A., Sherwood Lollar, B., DeFlaun, M., et al.  
840 (2005). Radiolytic H<sub>2</sub> in continental crust: nuclear power for deep subsurface microbial  
841 communities. *Geochemistry, Geophysics, Geosystems*, 6(7).

- 842 McCollom, T. M. (1999). Methanogenesis as a potential source of chemical energy for primary  
843 biomass production by autotrophic organisms in hydrothermal systems on Europa. *Journal of*  
844 *Geophysical Research: Planets*, 104(E12), 30729-30742.
- 845 McMahon, S., & Parnell, J. (2014). Weighing the deep continental biosphere. *FEMS*  
846 *Microbiology Ecology*, 87(1), 113-120.
- 847 McMahon, S., Parnell, J., & Blamey, N. J. (2016). Evidence for seismogenic hydrogen gas, a  
848 potential microbial energy source on Earth and Mars. *Astrobiology*, 16(9), 690-702.
- 849 National Institute of Standards and Technology (2021a), Stopping-power and range tables for  
850 helium ions, physics.nist.gov/PhysRefData/Star/Text/ASTAR.html.
- 851 National Institute of Standards and Technology (2021b), Stopping-power and range tables for  
852 electrons, physics.nist.gov/PhysRefData/Star/Text/ESTAR.html.
- 853 Nixon, S., Cousins, C. R., & Cockell, C. (2013). Plausible microbial metabolisms on  
854 Mars. *Astronomy & Geophysics*, 54, 1.13-1.16.
- 855 Lane, N., & Martin, W. F. (2012). The origin of membrane bioenergetics. *Cell*, 151(7), 1406-  
856 1416.
- 857 Preiner, M., Igarashi, K., Muchowska, K. B., Yu, M., Varma, S. J., Kleinermanns, K., et al.  
858 (2020). A hydrogen-dependent geochemical analogue of primordial carbon and energy  
859 metabolism. *Nature ecology & evolution*, 4(4), 534-542.
- 860 Radhakrishna, A.P., Somashekarappa, H.M., Narayana, Y., & Siddappa, K.A. (1993). New  
861 natural background radiation area on the southwest coast of India. *Health Physics* 65(4), 390-  
862 395
- 863 Schulte, M., Blake, D., Hoehler, T., & McCollom, T. (2006). Serpentinization and its  
864 implications for life on the early Earth and Mars. *Astrobiology*, 6(2), 364-376.
- 865 Sleep, N. H., Bird, D. K., & Pope, E. C. (2011). Serpentine and the dawn of life. *Philosophical*  
866 *Transactions of the Royal Society B: Biological Sciences*, 366(1580), 2857-2869.
- 867 Smetannikov, A. F. (2011). Hydrogen generation during the radiolysis of crystallization water in  
868 carnallite and possible consequences of this process. *Geochemistry International*, 49(9), 916-  
869 924. [Sonzogni and Shu, 2020] Sonzogni, A. and Shu, B. (2020), Nudat 2,  
870 www.nndc.bnl.gov/nudat2/.
- 871 Spinks, J. W. T., & Woods, R. J. (1990). *An Introduction to Radiation Chemistry*. New York:  
872 Wiley.
- 873 Stevens, T. O., & McKinley, J. P. (1995). Lithoautotrophic microbial ecosystems in deep basalt  
874 aquifers. *Science*, 270(5235), 450-455.



- 875 Tarnas, J. D., Mustard, J. F., Sherwood Lollar, B., Bramble, M. S., Cannon, K. M., Palumbo, A.  
876 M., & Plesa, A. C. (2018). Radiolytic H<sub>2</sub> production on Noachian Mars: implications for  
877 habitability and atmospheric warming. *Earth and Planetary Science Letters*, 502, 133-145.
- 878 Tarnas, J.D., Mustard, J.F., Sherwood Lollar, B., Stamenković, V., Cannon, K.M., Lorand, J.P.,  
879 et al., 2021. Earth-like Habitable Environments in the Subsurface of Mars. *Astrobiology*, 21(6),  
880 741–756.
- 881 Taylor, J.R. (1996). *An Introduction to Error Analysis: The Study of Uncertainties in Physical*  
882 *Measurements*, 2nd Edition., Sausalito, CA: University Science Books.
- 883 Waite, J. H., Glein, C. R., Perryman, R. S., Teolis, B. D., Magee, B. A., Miller, G., et al. (2017).  
884 Cassini finds molecular hydrogen in the Enceladus plume: evidence for hydrothermal  
885 processes. *Science*, 356(6334), 155-159.
- 886 Weaver, B. A., & Westphal, A. J. (2002). Energy loss of relativistic heavy ions in  
887 matter. *Nuclear Instruments and Methods in Physics Research Section B: Beam Interactions with*  
888 *Materials and Atoms*, 187(3), 285-301.
- 889 Webster, C. R., Mahaffy, P. R., Atreya, S. K., Flesch, G. J., Mischna, M. A., Meslin, P. Y., ... &  
890 Lemmon, M. T. (2015). Mars methane detection and variability at Gale  
891 crater. *Science*, 347(6220), 415-417.
- 892 Wentworth, C. K. (1922). A scale of grade and class terms for clastic sediments. *The Journal of*  
893 *Geology*, 30(5), 377-392.